

A pan-cancer dye for solid-tumour screening, resection and wound monitoring via short-wave and near-infrared fluorescence imaging

Received: 19 January 2024

Accepted: 21 July 2024

Published online: 09 September 2024

 Check for updates

Benedict Edward Mc Larney ¹, Ali Yasin Sonay ^{1,10}, Elana Apfelbaum ^{1,2,10}, Nermin Mostafa¹, Sébastien Monette ³, Dana Goerzen ^{1,4}, Nicole Aguirre⁵, Rüdiger M. Exner ⁶, Christine Habjan², Elizabeth Isaac^{1,2}, Ngan Bao Phung ^{1,2}, Magdalena Skubal¹, Mijin Kim ^{1,6}, Anuja Ogirala¹, Darren Veach ^{7,8}, Daniel A. Heller ^{1,2,4} & Jan Grimm ^{1,2,7,8,9} 

The efficacy of fluorescence-guided surgery in facilitating the real-time delineation of tumours depends on the optical contrast of tumour tissue over healthy tissue. Here we show that CJ215—a commercially available, renally cleared carbocyanine dye sensitive to apoptosis, and with an absorption and emission spectra suitable for near-infrared fluorescence imaging (wavelengths of 650–900 nm) and shortwave infrared (SWIR) fluorescence imaging (900–1,700 nm)—can facilitate fluorescence-guided tumour screening, tumour resection and the assessment of wound healing. In tumour models of either murine or human-derived breast, prostate and colon cancers and of fibrosarcoma, and in a model of intraperitoneal carcinomatosis, imaging of CJ215 with ambient light allowed for the delineation of nearly all tumours within 24 h after intravenous injection of the dye, which was minimally taken up by healthy organs. At later timepoints, CJ215 provided tumour-to-muscle contrast ratios up to 100 and tumour-to-liver contrast ratios up to 18. SWIR fluorescence imaging with the dye also allowed for quantifiable non-contact wound monitoring through commercial bandages. CJ215 may be compatible with existing and emerging clinical solutions.

Surgery is often the first and in the best-case scenario, the only treatment a cancer patient will undergo. Tumour surgery is constantly evolving but often relies on a surgeon's visual ability to innately determine tumour from healthy tissue under visible-light inspection. Fluorescence-guided surgery (FGS) improves tumour identification and delineation by visualizing fluorescent dyes accumulating in tumours. Fluorescence imaging and FGS are heavily utilized in a preclinical research setting but not yet widely adopted clinically, with

multiple barriers to be overcome by compounds and devices, particularly novel targeted ones¹. These limitations can include complicated agents, the lack of required clinical expertise and ultimately the need to show improved patient outcomes, despite the clinical dominance of optical techniques over other modalities². Targeted and even passive fluorophore accumulation imaged via FGS can dramatically improve a surgeon's capability to resect a tumour, aid in detecting smaller lesions, find lesions not identified by simple visual inspection, and locate lesions

A full list of affiliations appears at the end of the paper. ✉ e-mail: grimmj@mskcc.org

that have moved between the pre-op staging scans and the actual surgery (for example, through peristalsis)^{3,4}. With the advent of various FGS-based systems, especially those for robotic guided surgery, dyes that can readily be adapted to current clinical workflows are of the utmost importance¹. A tumour-selective antibody conjugated to a fluorophore of choice (for example, indocyanine green (ICG)) is the predominant approach for FGS, providing robust results, but is often only specific for a single-tumour type^{5–9}. Therefore, a novel compound must be developed for each tumour type to be targeted, preclinically tested and then subjected to clinical approval, in a temporally (over a decade) and financially (~US\$100–200 million) very costly process^{10,11}. The ‘by the minute’ charges for surgical room use (average of USD\$46.04 per min in 2022) where FGS requires additional time for the fluorescence imaging further hinders translation, preventing preclinically validated fluorophores from having the highest possible impact^{3,12,13}. FGS patients normally receive a single dose of the compound, and this (combined with the high costs of bringing such a compound to market) provides yet another barrier to translation^{10,14}. To overcome these hurdles, pan-tumour agents provide some of the highest value in biomedical cancer research, not only for FGS, utilizing for example, the known lower pH environment of most tumours¹⁵.

A long-established hallmark of cancer is apoptosis where unregulated cell reproduction and growth results ultimately in cellular damage and death since the tumour is outgrowing the available blood and thereby oxygen supply^{16–18}. Cellular damage and apoptosis are highest within the core of a tumour, where hypoxia and reduced blood flow form a non-sustainable environment^{19,20}. Efforts to clinically leverage this feature for FGS are overdue, with only few promising preclinical results so far^{21–24}. Current solutions have neither been clinically translated nor are they produced in larger quantities to match clinical doses. There is a clear demand for a scalable solution which should be easy to use, handle and administer. Importantly, a dye sensitive to apoptosis should have minimal uptake and therefore background in healthy tissue, improving tumour delineation via rapid clearance from non-diseased areas. This should inherently provide a pan-cancer targeting approach for numerous clinical applications, and potentially scenarios outside of tumour resection where apoptosis plays a role. Having multiple applications for a single dye could offset current market barriers and improve patient outcomes²⁵.

In this work, we investigated the delineation of multiple solid tumours and monitoring of wound healing *in vivo* via a single near-infrared (NIR)/short-wave infrared (SWIR)-emitting small-molecule dye, CJ215 (Proimaging, Paris). CJ215 is a commercial carbocyanine dye with a molecular weight of $-1,330 \text{ g mol}^{-1}$ and is inherently tumour targeting without antibody, peptide or ligand conjugation²⁶. CJ215 has a strong NIR fluorescence band (absorbance of 795–820 nm and peak emission at 810–840 nm, depending on the solution it is in) and, similar to ICG, extends to the SWIR region, potentially useful for short-wave infrared fluorescence imaging (SWIRFI) in clinical settings. We show cellular localization of CJ215 and its general *in vivo* tumour specificity. CJ215 was taken up in, and thus delineated, multiple preclinical solid tumour lines including breast (4T1, murine derived), prostate (PC3-PSMA, human derived), colon (CT26, murine derived), fibrosarcoma (HT1080, human derived) and peritoneal metastases of colorectal cancer (SW1222, human derived)^{27–30}. These models represent some of the most prevalent tumours, where surgery often is the primary treatment option (with or without adjuvant chemo/radiation therapy)^{31–35}. CJ215 tumour uptake could be detected with both SWIRFI and NIR fluorescence imaging (NIRFI). Signal to noise ratio (SNR) and contrast to noise ratio (CNR) assessment with SWIRFI were performed during screening and resection at $>900 \text{ nm}$ (sensor response) for all tumour lines and additionally at $>1,100$ and $>1,300 \text{ nm}$ long-pass cut-offs (via long-pass filters) for two tumour lines.

Since apoptosis is also a known component of wound healing, we therefore evaluated CJ215 for quantitative non-contact and

ambient-light-resistant longitudinal wound assessment through commercial bandages without removing them. CJ215 wound uptake and clearance was in agreement with reported healing timelines, with a repeat injection post healing not delineating the by-then healed wound^{36–38}. This work establishes CJ215 not only as a pan-cancer agent, which can delineate multiple solid tumours with a single systemic intravenous injection, but also as an agent with applications in general surgery. We further take advantage of the transparency of plastic compounds in the SWIR region to enable SWIRFI for wound assessment through bandages³⁹. This work also aids the establishment and translation of short-wave infrared fluorescence imaging in clinical domains, extending beyond FGS and also into post-operative care.

Results

Spectral characterization of CJ215

CJ215 is a small-molecule carbocyanine dye with a molecular weight of $-1,330 \text{ g}$ (Supplementary Fig. 1). First, we profiled the spectral absorption of CJ215 and determined whether it had any SWIR emission, as has been demonstrated for ICG and ICG-conjugated cancer targeting probes (Fig. 1a)^{6,40,41}. We found that CJ215 underwent a spectral red shift similar to that seen with ICG when suspended in fetal bovine serum (FBS) (Fig. 1a)⁴². This red shift in FBS was noted at a wide pH range of 4, 6, 7.4, 8 and 10, with CJ215 being highly stable in FBS over 150 min at all tested pHs but degrading rapidly (as shown by loss of absorption) in dextrose at a pH of 4 (Supplementary Fig. 2). CJ215 underwent further red shifting when suspended in either human serum albumin (HSA) or FBS at a pH of 7.4, followed by a slow blue shift of -5 nm in HSA or FBS over the course of 96 h (Supplementary Fig. 3). Little to no degradation (loss of absorption) of CJ215 was seen in both HSA and FBS. Although the NIR emission of the dye has been shown by the manufacturer, the SWIR emission and SWIRFI capability of the dye was yet unknown. To assess this, we dissolved CJ215 in dextrose, as well as in pure or diluted (in PBS) defibrinated sheep’s blood to simulate human blood (Supplementary Fig. 4). The peak absorption and emission of CJ215 red shifted by -25 nm in the presence of blood versus dextrose (794–818 and 813–838 nm, respectively), with SWIR emission extending to $-1,550 \text{ nm}$ (Fig. 1b and Supplementary Fig. 4). In addition, the dye underwent an increase in fluorescence intensity when present in serum or blood across this spectrum, further enhancing its suitability for *in vivo* imaging⁴³. We assessed the ability of SWIRFI to improve tumour delineation through scattering media, by imaging CJ215 through 5 mm of chicken breast (Supplementary Fig. 5). CJ215 was readily detected at 900 (indium gallium arsenide (InGaAs) sensor response lower cut-off), 1,000, 1,100, 1,200 and 1,300 nm long-pass cut-offs (achieved with long-pass optical filters), with delineation improving with extended (longer) wavelengths. This improvement is attributed to lower autofluorescence, insensitivity to excitation wavelength (808 nm) and reduced stray photon scatter via increased water absorption in this realm of the spectrum (Supplementary Fig. 5)^{44,45}.

In vitro assessment

Following characterization of the spectrum of CJ215, we assessed the level of CJ215 uptake *in vitro* in both 4T1 (murine breast cancer) and HT1080 (human fibrosarcoma) cell lines. We first assessed the subcellular localization of the dye via NIR point scanning confocal microscopy. After 3 h of incubation in 4T1 single cells and 3D spheroid structures, CJ215 was found to be localized to mobile vesicles inside the cells, likely taken up via endocytosis (Fig. 1c,d). To further assess the uptake of CJ215, 4T1 cells were incubated with the dye for 3 h at either 4 °C or 37 °C. As an energy-consuming process, endocytosis is impaired at 4 °C⁴⁶. Indeed, relative CJ215 uptake was reduced by 39.1% in cells at 4 °C, indicating that CJ215 is actively transported into cells (Fig. 1e). We also assessed the effect of inducing apoptosis via staurosporine (Sta), an apoptosis inducer, on CJ215 uptake in HT1080 (fibrosarcoma) cells. The addition of Sta increased relative CJ215 cellular uptake by 99% compared

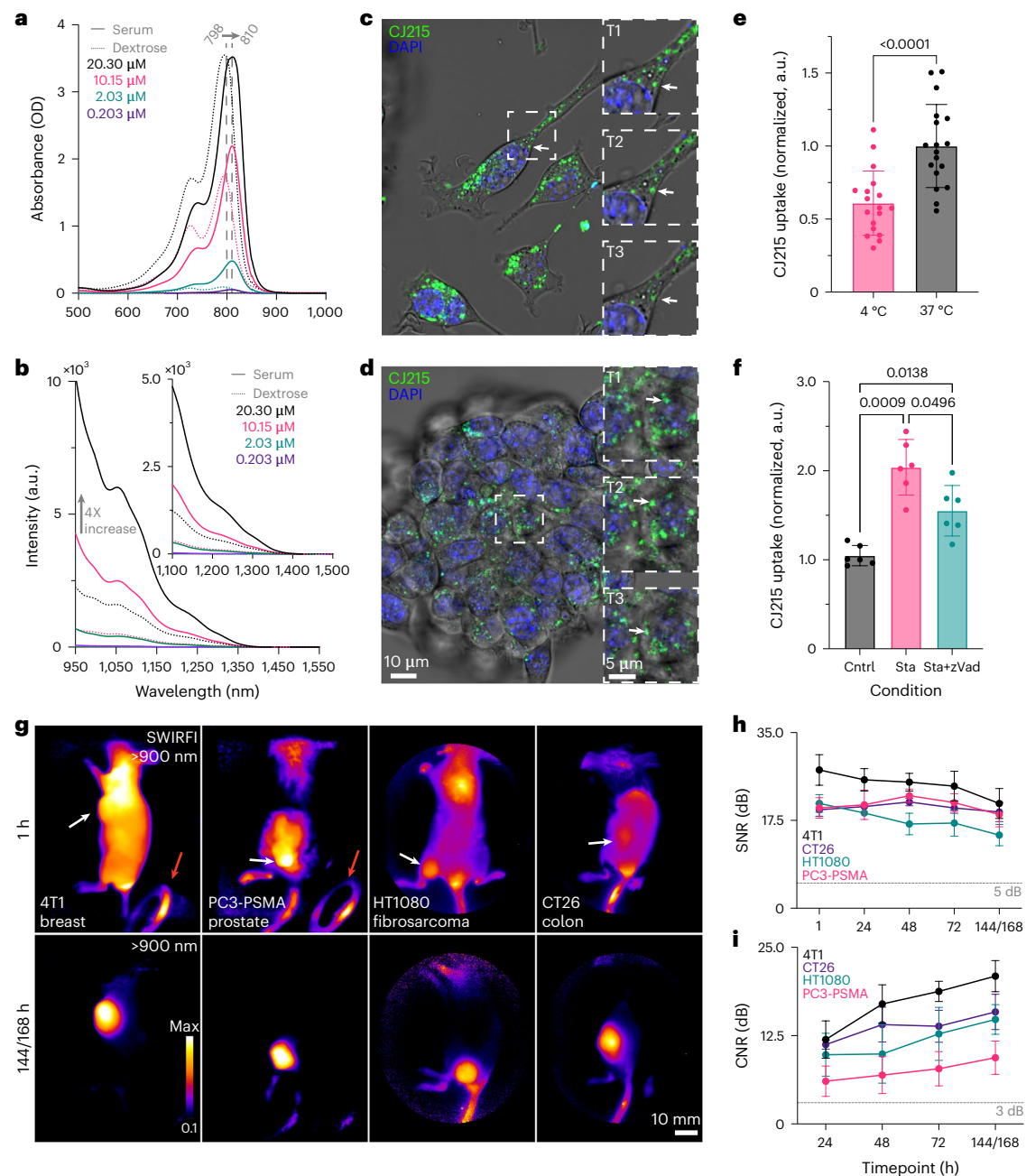


Fig. 1 | CJ215 spectral, in vitro and in vivo assessment. **a**, The absorption of CJ215 dissolved in either FBS (solid line) or dextrose (dotted line) was assessed at concentrations from 20.30 μM to 0.203 μM . The entire absorption spectrum red shifted in serum by 12 nm from a peak of 798–810 nm, similar to that of ICG. **b**, The SWIR emission tail of the dye was characterized from 950 to 1,550 nm with notable emission past 1,100 nm and a 4 \times increase in intensity when dissolved in serum vs dextrose. **c**, Representative single-cell NIR confocal microscopy localization uptake of CJ215 (green, 3 h incubation period) in 4T1 cells stained with DAPI (nucleus) with polarized white-light images overlaid (greyscale). Inset: zoom-in of vesicles containing CJ215 and their transport within the cell highlighting vesicle localization (T1 = 0 s, T2 = +23.175 s, T3 = +38.625 s). **d**, Representative Z-stack slice of CJ215 uptake in 4T1 spheroids (green, 3 h incubation period). Inset: zoomed-in image highlighting vesicle transport over time (T1 = 0 s, T2 = +17.962 s, T3 = +35.924 s). Supplementary Videos 1 and 2 further show vesicle transport. **e**, CJ215 uptake in 4T1 cells is based on active transport, with cells incubated with the dye at 37 $^{\circ}\text{C}$ showing a statistically significant increase (39.067%, Welch's two-sided unpaired parametric *t*-test) in uptake compared with those incubated with CJ215 at 4 $^{\circ}\text{C}$; mean \pm s.d., $n = 18$ technical replicates from $n = 3$ biological replicates (6-well plates). **f**, Cell damage and apoptosis induction by staurosporine (Sta) statistically significantly

increases CJ215 uptake in HT1080 cells by 99.298% compared with control cells. zVad-FMK (zVAD, an apoptosis blocker) combined with Sta reduced maximum uptake (48.826%) compared with Sta alone. Mean \pm s.d. and replicates (dots) shown; non-paired or matched Welch and Brown–Forsythe analysis of variance (ANOVA) with Dunnett's T3 multiple comparisons test. **g**, Ambient-light-resistant SWIRFI-based (>900 nm) screening of four tumour cell lines including 4T1 (breast, orthotopic, murine), PC3-PSMA (prostate, heterotopic, human), HT1080 (fibrosarcoma, orthotopic, human) and CT26 (colon, heterotopic, murine). Top: representative images of all tumour lines at 1 h post intravenous systemic injection of CJ215. Fluorescence reflections are visible in the ambient lighting LED (red arrow, circular object in bottom right). Bottom: images of tumour uptake and localization of CJ215 at 144 or 168 h post injection at video rate exposures (1–2 ms). In all cases, the tumour can be readily delineated. **h**, SNR (dB) quantification of all tumour lines. At all timepoints, sufficient SNR is achieved above the 5 dB threshold, with exposure times ranging from 1–2 ms (808 nm excitation, $\sim 300 \text{ mW cm}^{-2}$). **i**, CNR (dB) quantification for all tumours and all mice, where sufficient contrast is achieved (above 3 dB threshold) at 24 h post injection, with CNR steadily increasing up to 144/168 h for all tested tumour lines. In all cases, the mean (dot) and s.d. are shown from $n = 4$ mice per tumour line ($n = 16$ mice total), aside from the 24 h HT1080 line where only $n = 3$ mice achieved sufficient CNR.

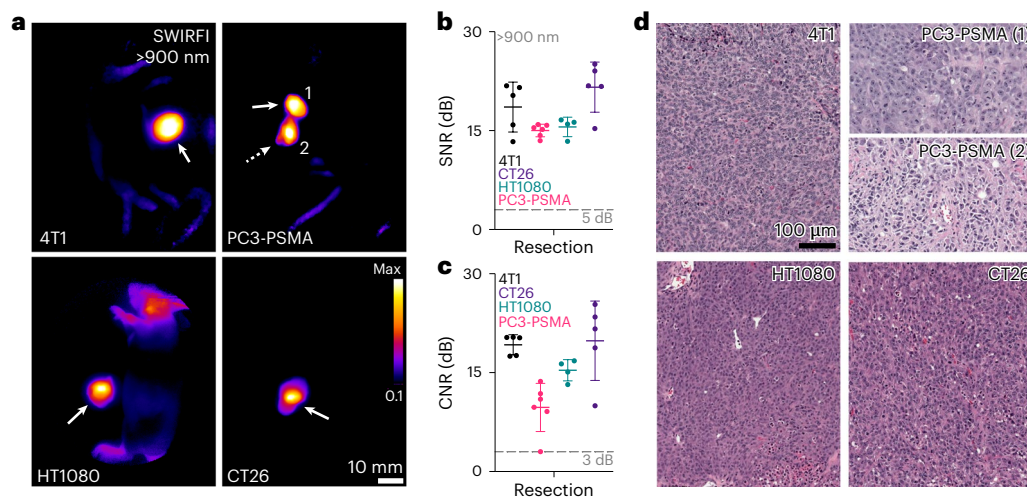


Fig. 2 | Tumour resection using SWIRFI (>900 nm, sensor response) and CJ215. a, Resection confirmation of various tumours in euthanized mice. In all cases, the primary tumour site is highlighted by the solid arrow, with remnant lesions highlighted by the dotted arrow. In the PC3-PSMA cohort, resection was performed twice on one mouse to completely resect all fluorescent areas (1, 2). **b**, SNR quantification of all resected lesions, with sufficient SNR achieved in all cases (>5 dB threshold). **c**, CNR quantification of all resected lesions, with sufficient CNR achieved for all primary tumour sites in all cases (>3 dB threshold).

In all cases, the mean, s.d. and each replicate (dots, $n = 4$ mice per tumour line, up to 6 dots includes secondary sites when present) are shown for all tumour lines. Statistical comparisons were not performed as all tumours fulfilled SNR and CNR thresholds. **d**, H&E staining of tumour areas removed during resection; images shown at $\times 20$ magnification. All fluorescent areas were confirmed to be tumourous as characterized by the high density of nuclei. For the remnant PC3-PSMA tumour (2) removed during R2, this was determined as residual primary tumour tissue below the skin surface.

with untreated control cells, while the addition of a caspase inhibitor (carbobenzoxy-valyl-alanyl-aspartyl-[*O*-methyl]-fluoromethylketone, zVAD FMK), which inhibits Sta-induced apoptosis, reduced that uptake by 48.8% (still relatively increased to 51.1% of control) compared with Sta alone (Fig. 1f)⁴⁷. Importantly, ICG incubation under comparative conditions did not yield any statistically significant change in cellular uptake (Supplementary Fig. 6). Finally, we found that serum-starved 4T1 cells had a 54.3% higher uptake of CJ215 than cells incubated in the presence of serum, as has been shown for other dyes (Supplementary Fig. 7)^{43,48}. Following fixation with formaldehyde, cells retained CJ215 fluorescence levels up to 9 days post fixation (Supplementary Fig. 8). To further confirm binding to apoptotic cells, we stained cells with dyes binding to the nucleus, lysosomes and plasma membrane together with CJ215 (Supplementary Fig. 9) and found that in cells which appeared morphologically apoptotic, CJ215 showed moderate correlation with the plasma membrane (mean Pearson's $R = 0.38 \pm 0.04$ (s.d.), $n = 4$ technical replicates from $n = 1$ experiment), while it showed no or weak co-localization with either the nucleus or lysosomes (mean Pearson's R of 0.01 ± 0.03 and 0.10 ± 0.12 , respectively, $n = 4$ technical replicates from $n = 1$ experiment).

In vivo screening

Having determined that induction of apoptosis increased cellular uptake of CJ215 and that the dye was predominantly taken up by cells via active transport, we next assessed CJ215's capability for preclinical tumour screening across four tumour lines in mice implanted with a single lesion site. With lower apoptosis levels found in healthy/normal tissues, we hypothesized that tumours would be the main site of CJ215 retention. We utilized a SWIRFI system equipped with an 808 nm laser (300 mW cm^{-2}) to assess CJ215 uptake in male and female mice, across FoxNI^{nu}, SCID and BALB/c mouse lines under ambient lighting conditions⁴¹. The tested tumour lines comprised xenografted mice bearing breast (4T1, murine, orthotopic), prostate (PC3-PSMA, human, heterotopic), HT1080 (fibrosarcoma, human, orthotopic) and CT26 (colon, murine, heterotopic) tumours (Fig. 1g). All mice were imaged every 24 h from 1 to 96 h and finally at a late timepoint of 144 or 168 h post injection (Fig. 1h). The SWIRFI system (>900 nm, sensor response) enabled

video rate (30 Hz) acquisitions under ambient lighting conditions and readily achieved sufficient SNR (>5 dB) at all tested timepoints, with exposure times as low as 1 ms (Fig. 1h). In all cases, the dye showed highly selective tumour uptake, with sufficient SNR achieved within 1 h post injection. Contrast (CNR), the ability to delineate the tumour from healthy tissue, achieved sufficient levels (>3 dB, Rose criterion) from 24 to 168 h, with CNR increasing with increasing clearance time (Fig. 1i)^{49,50}. Images from all mice at all timepoints are also presented (Supplementary Figs. 10–13). All SWIRFI presented throughout this work was performed with the ambient lighting LED on, at no detriment to image fidelity⁴¹.

Tumour resection

Post-euthanasia tumour resection was confirmed in all mice using SWIRFI under ambient lighting conditions. The assumed primary tumour was resected, and both the excised tumour and tumour bed (remaining tissue, that is, the mouse body) were placed side by side within the SWIRFI system (Fig. 2a). In all cases, the primary site contained enough fluorescence to delineate the tumour while also confirming that the tumour bed was free of residual fluorescence. If suspected remnant tumour was left behind, as noted by a highly fluorescent area, this was then resected. For all tested tumours, the primary and potential secondary sites had sufficient SNR (Fig. 2b) for detection, along with sufficient CNR (Fig. 2c) to be delineated from the tumour bed site. Resection images for all mice and all tumours are also shown (Supplementary Figs. 14–17).

Extended spectral emission of CJ215 assessment

The extended spectral emission of carbocyanine dyes into the SWIR spectrum, which only SWIRFI systems can detect, provides improvements in delineation and resolution, especially through scattering media^{44,51}. We compared the extended spectral emission of CJ215 in HT1080 and CT26 tumour uptake at >900 (sensor response), >1,100 and >1,300 nm (via long-pass optical filters). This was performed to assess increased resolution, delineation and penetration via water absorption, which begins to increase at >1,100 and further increases at >1,300 nm (Supplementary Fig. 5)⁴⁵. In all cases, CJ215 could be detected but as expected, required increasingly longer exposure times at longer

wavelength cut-offs (1–2 ms for >900 nm, 100–200 ms for >1,100 nm and 500–1,500 ms for >1,300 nm cut-offs). Tumour SNR was sufficient at all timepoints, with CNR permitting tumour delineation for HT1080 tumours at 1 h but not for the CT26 line (Supplementary Fig. 18). Data combined from both lines permitted a clearer SNR and CNR assessment and comparison between timepoints. The effect of these cut-offs for resection efficacy was also assessed in both primary sites and potential secondary locations (Fig. 3a). In all cases, the >1,300 nm cut-off provided the lowest SNR and CNR, with >1,100 and >900 performing comparably (Fig. 3b,c). A similar trend was identified for screening (Supplementary Fig. 18). However, the >1,300 nm cut-off did improve delineation of the tumour core for both tested tumour lines (Fig. 3a,e,f). We found that dye localization and core delineation improved both qualitatively and quantitatively at longer wavelengths, most obviously at 1,300 nm (Fig. 3e,f). Using immunohistochemistry (IHC) for cleaved caspase 3 (CC3, a known apoptosis marker), we confirmed that the core of the tumours had the highest levels of apoptosis, with increased apoptosis observed throughout the tumour (Fig. 3g)⁵².

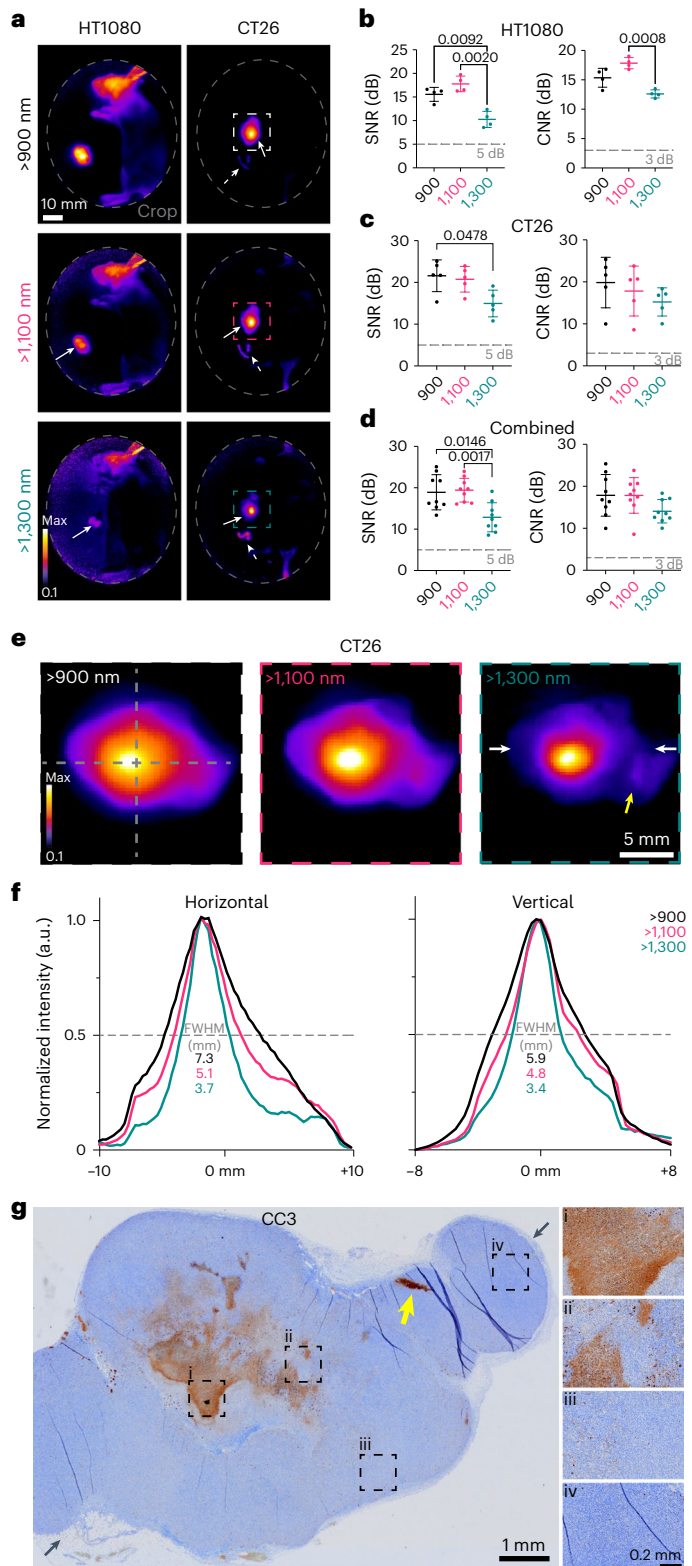
CJ215 biodistribution

While SWIRFI is an emerging technique with advantages over established methods, due to the unavailability of SWIRFI systems, it remains a restricted resource to many researchers with even fewer clinical options. In addition, the SWIRFI system employed here had a relatively small field of view (FOV), limiting simultaneous imaging of multiple organs. To highlight the suitability of CJ215 for conventional NIRFI, the IVIS Spectrum system (silicon-based sensor) was utilized for biodistribution assessment⁵³. Resected organs were imaged simultaneously with fluorescence levels, then quantified to highlight the various tumour to organ ratios. In all cases, the tumour was always the brightest tissue, achieving tumour:muscle ratios of up to 99.63 (Fig. 4). For nearly all models, minimal to no remnant uptake was seen in healthy tissues, resulting in, for example, tumour:spleen ratios of up to 47.7 or tumour:liver ratios of 17.86 (Fig. 4). Residual fluorescence seen in the kidneys highlights the renal clearance of CJ215. Biodistributions from all tumours and all mice are shown in Supplementary Figs. 19–26, along with corresponding haematoxylin and eosin (H&E) staining of select organs.

Fig. 3 | Extended spectral emission (>1,100, >1,300 nm) assessment of CJ215 via SWIRFI.

a, Extended spectral emission assessment of CJ215 and SWIRFI for resection at >900 (spectral response of the sensor), >1,100 and >1,300 nm cut-offs (long-pass optical filters) for HT1080 and CT26 tumour lines. Note, the core of the tumour becomes most prominent at >1,300 nm. Non-specific uptake (lymphatic) is seen in the head of the HT1080 mouse. Primary tumour sites are highlighted (solid arrow) along with suspect secondary sites (dotted arrows). Dashed gray circles represent post processing cropping performed due to the use of an optical filter at longer wavelengths. **b**, SNR and CNR quantification of the HT1080 tumour line, with >1,100 nm presenting the highest contrast but not statistically significant improvement over >900 nm. **c**, SNR and CNR quantification of the CT26 tumour line, with no difference found in CNR between tested cut-offs. **d**, Combined assessment of HT1080 and CT26, with >1,300 nm found to provide the lowest SNR compared with other cut-offs, with no statistically significant difference in CNR found when combining both groups. In all cases, the mean, s.d. and replicates are shown ($n = 4$ per tumour line, $n = 8$ for combined); non-paired or matched Welch and Brown–Forsythe ANOVA with Dunnett’s T3 multiple comparisons test. Thresholds are shown as before (5 dB and 3 dB for SNR and CNR, respectively). **e**, Zoomed-in view of the CT26 tumour at 900, 1,100 and 1,300 nm. **f**, Vertical and horizontal full width at half maximum (FWHM) assessment (dashed grey lines) of the tumour at all wavelengths. The qualitative improvement in tumour core delineation seen at >1,100 and best at >1,300 nm is also observed quantitatively. **g**, Corresponding CC3 immunohistochemistry staining of the CT26 tumour shown in **a** and **e**, showing highest levels of apoptosis at the tumour core with positively stained cells present throughout the sample (i–iv). Black arrows show the approximate slice location and the yellow arrow indicates an apoptotic tumor nest that becomes visible of SWIRFI at 1,300 nm corresponding to the yellow arrow and white arrows in **e**.

Following the resection of CT26 tumours, notable residual fluorescence was determined adjacent and in proximity to the resected tumour beds of two mice (M3, M4) (Fig. 5a). These areas were also resected (Fig. 5b; region of interest (ROI)-2) and sent with the primary tumour and select organs for histological analysis (Fig. 5c–e). When compared with tumour tissue, these tissues had lower CJ215 uptake yet were still elevated over other organs and were found to be tumour free. These areas were identified as small intestine, lymph node, uterine and ovarian



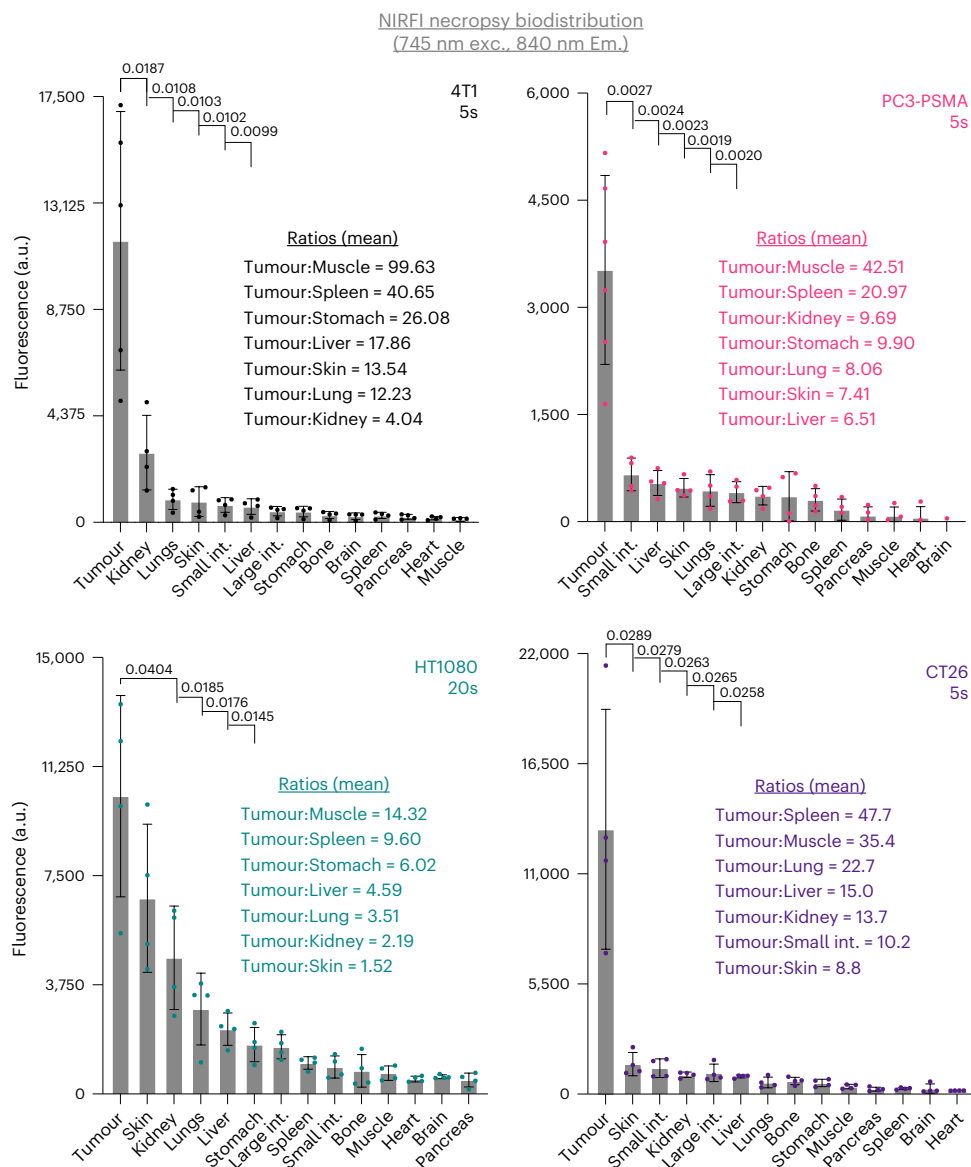


Fig. 4 | NIRFI (745 nm excitation, 840 nm emission) necropsy biodistribution assessment of CJ215 in four tumour models. Following resection, various organs were collected for necropsy-based biodistribution assessment via NIRFI (IVIS Spectrum, 745 nm excitation, 840 nm emission) at exposure times of 5–20 s. Tumours had the highest level of uptake in all tumour models. Residual kidney

fluorescence identifies renal clearance of CJ215. Organs are shown in order of decreasing fluorescence intensity with notable tumour/organ ratios shown. Select *P* values from unpaired parametric Welch's *t*-test comparing tumour to organs; mean \pm s.d., individual replicates shown as dots; $n = 4$ mice.

tissue with the additional focus in M3 containing a small tumour fragment. Further, IHC staining for CC3 (Fig. 5d), found increased levels of apoptosis in these tissues. As expected, CT26 primary tumour sites had highly elevated levels of CC3-positive cells, especially within the core of the tumour (Supplementary Fig. 27). The additionally resected tissues that had increased CJ215 fluorescence also displayed increased levels of CC3-positive cells (Fig. 5e)⁵². Importantly, we found a similar trend in tumour delineation and biodistribution (for example, tumour:muscle ratio of 9.74) at 48 h post injection of CJ215 in 4T1 bearing mice, with dye uptake correlating with CC3+ staining (Supplementary Figs. 28 and 29). An additional batch of mice bearing 4T1 tumours (xenografted as before) were intravenously administered ICG (suspended in dextrose in the same manner as CJ215) but ICG failed to delineate all tumours and was not able to sufficiently confirm tumour resection (Supplementary Figs. 30 and 31). Further, ICG showed little to no tumour retention at later timepoints based on biodistribution data or retention in tumours that were apoptotic (CC3+) (Supplementary Figs. 32 and 33).

Contrast-based SWIRFI for binary tumour delineation

Having determined that simply letting CJ215 clear from healthy tissues improved tumour delineation, we utilized further image processing to improve tumour delineation. This was done with the goal of presenting a surgeon with an efficient way to display the images when using CJ215, based on their selection of a non-tumour background reference point. The entire process was completed using ImageJ at a rate of 3.78 ms per frame with the chosen region recorded, the mean and s.d. of the ROI calculated, followed by respective framewise correction according to widely established CNR calculations (see equation 1). The resulting image was then displayed as a *contrast-based image* expressed in CNR (dB), dubbed 'contrast mode' (Fig. 6a). SWIRFI and CJ215 CNR images can readily provide a surgeon with binary tumour delineation, with a 3 dB threshold (Rose criterion) found to be effective for all tested tumour lines as seen in Fig. 6b. This method was also implemented on a pixelwise method but performed less efficiently (25.5 ms per frame) with no discernible difference in CNR outputs (Supplementary Fig. 34).

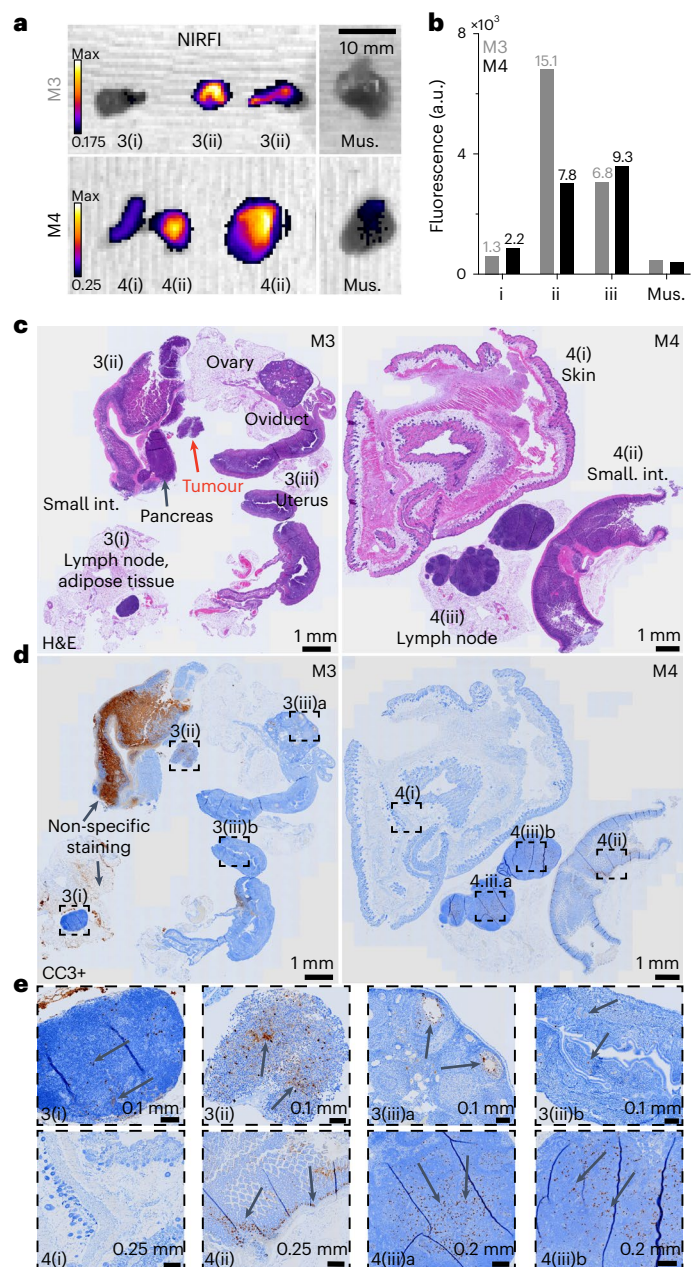
$$\text{Pixel}_{\text{New}} = \left(\frac{\text{Pixel}_{\text{Old}} - \text{ROI}_{\text{Mean}}}{\text{ROI}_{\text{s,d}}} \right) \quad (1)$$

Assessment of CJ215 in a metastatic tumour model. The four tumour models used herein are readily and widely utilized for the assessment of tumour targeting of both fluorescent, radioactive and treatment agents. However, these models represent a single tumour location under the skin surface, where CJ215 and most other optical agents can be readily visualized, not faithfully modelling the clinical reality. A more challenging location presenting an urgent clinical problem is peritoneal carcinomatosis and its surgical removal (debulking)^{54,55}. SW1222 is a highly aggressive human colorectal carcinoma tumour line, which spreads throughout the peritoneal space. This heavily invasive and often palliative debulking surgery requires organ extra corporation where organs are inspected *ex situ*. The peritoneal cavity is then also inspected using white-light investigation for remnant tumour. This procedure would benefit considerably from a suitable targeted dye for FGS. Our model of metastatic peritoneal spread consisted of SW1222 luciferase expressing patient-derived xenografts of colorectal cancer cells injected intraperitoneally⁵⁵. Once sufficient tumour burden was confirmed using bioluminescence imaging, animals were administered with CJ215 as before. SWIRFI was performed at >900, >1,100 and >1,300 nm cut-offs to assess tumour screening. Tumour visualization of the SW1222 model without previous knowledge of lesion location was initially difficult to achieve over endogenous colon signal (Fig. 7a–c and Supplementary Fig. 35). As before, necropsy biodistribution was performed with NIRFI at 168 h post injection, showing improved tumour delineation after organ isolation (Fig. 7d and Supplementary Fig. 35). We found that tumours were widely dispersed throughout the peritoneum and highly necrotic, with patchy fluorescence seen across identified tumours (Fig. 7b,c). In all mice, highly fluorescent lesions were seen adjacent to the spleen, engulfing the pancreas (Panc. tum.) (Fig. 7d), and were confirmed to be tumourous via H&E staining (Fig. 7e and Supplementary Fig. 36). Highly necrotic tumours still achieved a tumour:muscle ratio of 7.89 (Fig. 7d). Pancreatic tumours had an improved tumour:muscle ratio of 10.38 and 8.80 over the adjacent spleen (Fig. 7d), appearing less necrotic (H&E staining; Fig. 7e), highlighting the ability of CJ215 to delineate organ-bound tumour masses and uptake in viable tumours during debulking approaches.

Fig. 5 | Necropsy and histological analysis of additional regions of interest during CT26 tumour resection. **a**, During CT26 resection and necropsy, small areas (labelled as 3(i), 3(ii) and so on) were identified and found to be highly fluorescent (NIRFI, IVIS Spectrum, 745 nm excitation, 840 nm emission) over background areas and muscle tissue. **b**, Quantification of ROIs with ROI:muscle ratios shown above bars. **c**, Left: H&E staining of resected tissues from M3 identified (clockwise) as a lymph node surrounded by adipose tissue (3(i)), the small intestine with pancreas and a small tumour area not bound to any identifiable tissue (3(ii)) and finally, the reproductive organs including the uterus, oviduct and ovaries (3(iii)). Right: H&E staining of resected tissues from M4 identified (clockwise) as the skin and subcutis (4(i)), the small intestine with adipose tissue (4(ii)) and finally, a lymph node also surrounded by adipose tissue (4(iii)). **d**, CC3+ (for apoptosis, that is, damaged cells) IHC staining on a consecutive slice for each mouse sample. Labelled dashed boxes highlight ROIs with increased levels of CC3-specific staining. Non-specific CC3 staining widely seen in the small intestine of M3 should be ignored. **e**, Zoomed-in areas as highlighted at various magnification levels: 3(i), small to moderate number of CC3+ cells were seen in the lymph node cortex and paracortex; 3(ii), CC3+ cells were found in the tumour region; 3(iii)a, CC3+ cells are highlighted in the granulosa of ovarian follicles; 3(iii)b, small number of CC3+ cells were seen within the endometrial epithelium. 4(i), no CC3+ cells were seen in the skin; 4(ii), moderate number of CC3+ cells were seen within the crypts, with a small number in the enterocytes of villi; 4(iii)a,b, small to moderate number of CC3+ cells were seen throughout lymph node cortex and paracortex.

Wound monitoring

During hair depilation in the CT26 model, slight skin surface damage was inadvertently instigated, which then proceeded to form scabs and heal over time. We incidentally noticed high levels of CJ215 uptake in these areas, along with tumour uptake (Supplementary Fig. 37). Over the 168 h imaging period, the wound fluorescence decreased with progressing wound healing while tumour fluorescence persisted. Spurred on by this finding, we assessed the ability of SWIRFI to image CJ215 through a variety of commercially available bandages (Supplementary Fig. 38). SWIRFI readily detected CJ215 through all tested bandages, the majority of which were opaque in visible light. Encouraged by this observation, we next implemented a controlled wound monitoring experiment where mice underwent a skin incision with a scalpel, followed by absorbable stitch closing. These mice received CJ215 intravenously and hydrogel burn bandages were placed over the wound during imaging. These provided a non-stick barrier at the wound site, are highly scattering, hindering visible-light wound inspection, and delivered suitable intensity losses and SNR changes in phantom testing (Supplementary Fig. 38). Mice were imaged at >900, >1,100 and



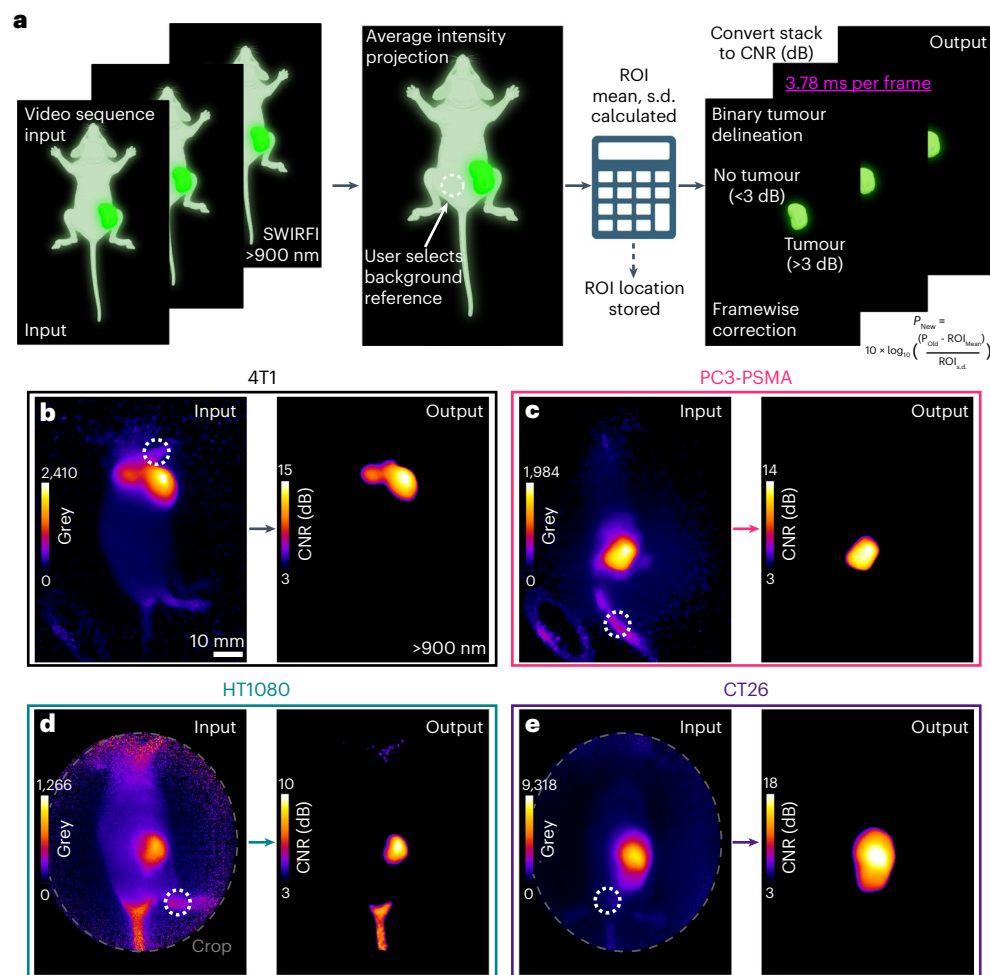


Fig. 6 | SWIRFI (>900 nm) and CJ215 enable contrast-based image generation for binary tumour delineation. **a**, Schematic describing the frame-wise computation of contrast images, based on user input with >900 nm SWIRFI images. Created with Biorender.com. **b–e**, Representative SWIRFI input and output images for all tested tumour lines at >900 nm. The CNR threshold of 3 dB was found to be effective for all tumour lines at the 144/168 h timepoints.

The white dotted circle represents the user chosen background reference point. Presented images are single frames from post-processed (corrected) video rate acquisitions. Video sequences based on a per-pixel method are available in Supplementary Video 3 (see also Supplementary Fig. 34). Non-specific uptake is present at the tail of the HT1080 mouse, but the tumour is delineated over surrounding tissue.

>1,300 nm with and without a bandage from 2 to 240 h (10 days) post surgery and CJ215 injection (Fig. 8a,b and Supplementary Figs. 39–42). The bandage was only placed on mice during imaging and was removed before they awoke to prevent discomfort to mice, inadvertent bandage consumption, or bandage degradation. We found that after a single injection of CJ215, the intensity of dye uptake corresponded with wound healing progression using CNR as a metric for wound assessment, with >1,300 nm providing the best wound CNR, along with the wound being readily delineated through the bandage during the main healing phase (Fig. 8c). The reduction in signal by the bandage prevented reliable wound delineation at 168 h and onwards since uptake decreased in healing wounds. Wound CNR was detectable from 1–2 h post injection, highlighting the quick uptake and localization of CJ215 to wounds. CNR peaked at 48 h post injection, then dropped over time until the wound was no longer detectable (that is, completely healed), with longer exposure times utilized between 72 and 240 h post injection to ensure sufficient signal collection. CNR was found to provide a quantitative metric for wound healing assessment in line with visible-light inspection of wound healing but, importantly, is also usable when removal of wound dressing is detrimental to the patient (for example, in burn victims). To confirm lack of wound uptake once healed, mice then received a second injection of CJ215 and were imaged every 24 h from 1 to 48 h

post injection. As opposed to imaging following the surgery, sufficient contrast could not be detected within the now-healed wound region in all mice, with necropsy-based biodistribution showing no statistically significant difference in fluorescence intensity in the wound area versus normal skin (Supplementary Fig. 43). H&E further confirmed the normal physiology of the wound area (Supplementary Fig. 44).

Discussion

We have validated the use of the commercial carbocyanine dye, CJ215, for tumour delineation in preclinical cancer models as well as monitoring of naïve and dressed wounds. CJ215 fulfils many requirements for clinical translation and, importantly, behaves optically similar to ICG and is therefore compatible with the wide array of already existing clinical FGS systems (Fig. 1a). CJ215 can take advantage of the reduced optical tissue scatter and absorption in the NIR, which, aside from its US Food and Drug Administration (FDA) approval, explains the dominance of ICG. Furthermore, CJ215 has a strong emission tail into the SWIR (Fig. 1b), which provides advantages over NIR and visible emission ranges⁴⁴. We set out to elucidate the potential tumour targeting capability of CJ215 by assessing its uptake *in vitro*. CJ215 appeared to be endocytosed and spread across multiple mobile vesicles within 4T1 single cells and spheroids (Fig. 1c,d, and Supplementary Videos 1 and 2).

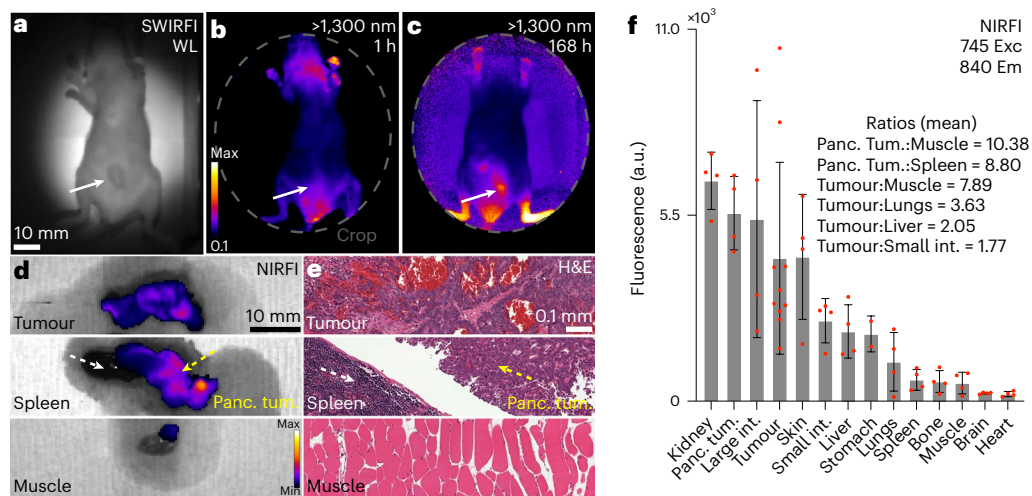


Fig. 7 | CJ215 assessment in a colorectal peritoneal carcinomatosis model (SW1222). **a**, SWIR reflection image (940 nm) of a mouse bearing SW1222 within and protruding through the peritoneum (white solid arrow). **b**, Image at $>1,300$ nm at 1 h post CJ215 administration. **c**, Image at $>1,300$ nm at 168 h post CJ215 administration. **d**, Representative NIRFI (840 nm) necropsy image of select organs (M4) including a representative large tumour mass found throughout the peritoneal space, the spleen (dashed white arrow), a tumour mass on the pancreas (dashed yellow arrow) and muscle tissue. **e**, Representative H&E staining of the tissues shown in **b** confirming necrotic regions present in the

larger tumour mass, normal spleen and pancreatic tumour (less necrosis than the large tumour mass), and muscle tissue. **f**, Quantification of dye distribution in the SW1222 model. Select tumour:organ ratios are provided, with CJ215 highlighting its renal clearance. Pancreatic tumour masses were quantified separately and compared to both the spleen and muscle tissue. Organs are organized in order of decreasing fluorescence intensity with select ratios; mean \pm s.d., individual replicates shown as red dots; $n = 4$, except for the stomach data where two negative (below 0) values were excluded.

CJ215 uptake is increased in cells that are actively metabolic, as shown by the incubation at 4°C vs 37°C (Fig. 1e). We show that induction of apoptosis (cell death) with staurosporine doubled relative cellular uptake of CJ215 in HT1080 cells, while apoptosis inhibition tempered this uptake, indicating that the dye is more readily taken up by apoptotic cells (Fig. 1f)⁴⁷. Notably, in the presence of FBS (serum), cellular uptake of CJ215 was reduced by over 50%, that is, starved cells took up CJ215 more avidly (Supplementary Fig. 7). CJ215 was found to be stable (still fluorescent) in cells post fixation with formaldehyde over the course of days (Supplementary Fig. 8).

CJ215 showed excellent uptake in a variety of in vivo tumour models representing some of the most prevalent cancers including breast (4T1), prostate (PC3-PSMA), fibrosarcoma (HT1080) and colon (CT26) cancer (Fig. 1g). High uptake was seen in all models across multiple mouse lines, both in male and female mice, with human and murine-derived tumours in various orthotopic and heterotopic locations (Fig. 1g). Our previously established ambient-light-resistant SWIRFI method and CJ215 could delineate tumours as early as 1 h post injection, with highly conclusive delineation at 24–168 h (Fig. 1h,i)⁴¹. This ambient lighting setup—potentially preferred by surgeons as it avoids constant switching of light sources and adaptation to new light intensities—is based on an RGB LED with a similar fluence to shadowless surgical lighting ($70 \mu\text{W cm}^{-2}$ where current surgical systems provide 10 – $170 \mu\text{W cm}^{-2}$ at 488 nm)^{41,56}. Tumour contrast steadily increased over time, in line with previous investigations with other carbocyanine-based probes (Fig. 1i)⁴¹. Tumour resection performed on euthanized mice found that SWIRFI with CJ215 enabled confirmation of tumour resection, informed on remnant tumour and highlighted other suspect regions, with the tumour site always having the brightest fluorescence (Fig. 2). We also found a favourable biodistribution with retained tumour uptake and clearance from other organs at 48 h post injection of CJ215 (Supplementary Figs. 28 and 29).

To further confirm the utility of CJ215, we performed a similar experiment with ICG-injected 4T1 tumour bearing mice in the same manner, imaged and analysed as for CJ215 experiments. Under comparative conditions, ICG failed to successfully delineate all tumours ($n = 3$ mice) and was hindered by high liver and excretion fluorescence

levels (Supplementary Figs. 30 and 31). For the one tumour that was detected via ICG, this was achieved at a reduced SNR and CNR level (-10 dB loss for each at 1 ms exposure). ICG further failed to provide conclusive resection confirmation in conjunction with a poor bio-distribution profile, even when compared to the worst-performing CJ215 data (HT1080) (Supplementary Fig. 32). The tumours were found to also be apoptotic, with a necrotic core confirmed via H&E and CC3 staining (Supplementary Fig. 33). Notably, the molecular weight of ICG is almost half of that of CJ215 (775 g mol^{-1} vs $1,330 \text{ g mol}^{-1}$, respectively). Accordingly, the ICG-injected mice received -1.7 -fold increase in molecular dosage at 2 mg kg^{-1} and yet, ICG still failed to perform as well as CJ215.

SWIRFI enabled investigation of the extended spectral emission of CJ215, which current silicon-based sensors cannot detect (Supplementary Fig. 5)^{6,40,51}. We assessed the reduction in photon scatter of CJ215 by increased water absorption at $>1,100$ and $>1,300 \text{ nm}$ long-pass cut-offs to improve tumour CNR (Fig. 3). For both screening and resection, these wavelengths did not provide a major advantage in tumour delineation due to the high tumour uptake of CJ215 and the suboptimal video rate imaging at these longer wavelengths (Fig. 3b–d). However, the $>1,300 \text{ nm}$ cut-off provided both qualitative and quantitative non-destructive insight to CJ215 distribution within the tumour core, highlighting tumour heterogeneity (Fig. 3e,f). This core uptake was reflected in CC3 (apoptosis) staining via IHC, confirming the observations made via SWIRFI (Fig. 3e,g).

SWIRFI has optical benefits but remains a novel and often inaccessible tool due to limited access to suitable imaging equipment. The utilized SWIRFI system has a reduced FOV (a single mouse), making multiple organ comparisons cumbersome. We performed NIRFI necropsy biodistribution post resection on an IVIS system with a larger FOV (up to 5 mice), further confirming both CJ215 tumour localization and suitability for NIRFI (Fig. 4). Tumours had the brightest fluorescence in all experiments, with non-tumour bearing organs having minimal residual dye uptake. This biodistribution enabled unprecedented tumour:muscle ratios of up to 100 where anything above 2 or even 1.5 is considered successful (Fig. 4)⁵⁷. Furthermore, CJ215 cleared from vital organs such as the liver, spleen and pancreas, enabling tumour:organ

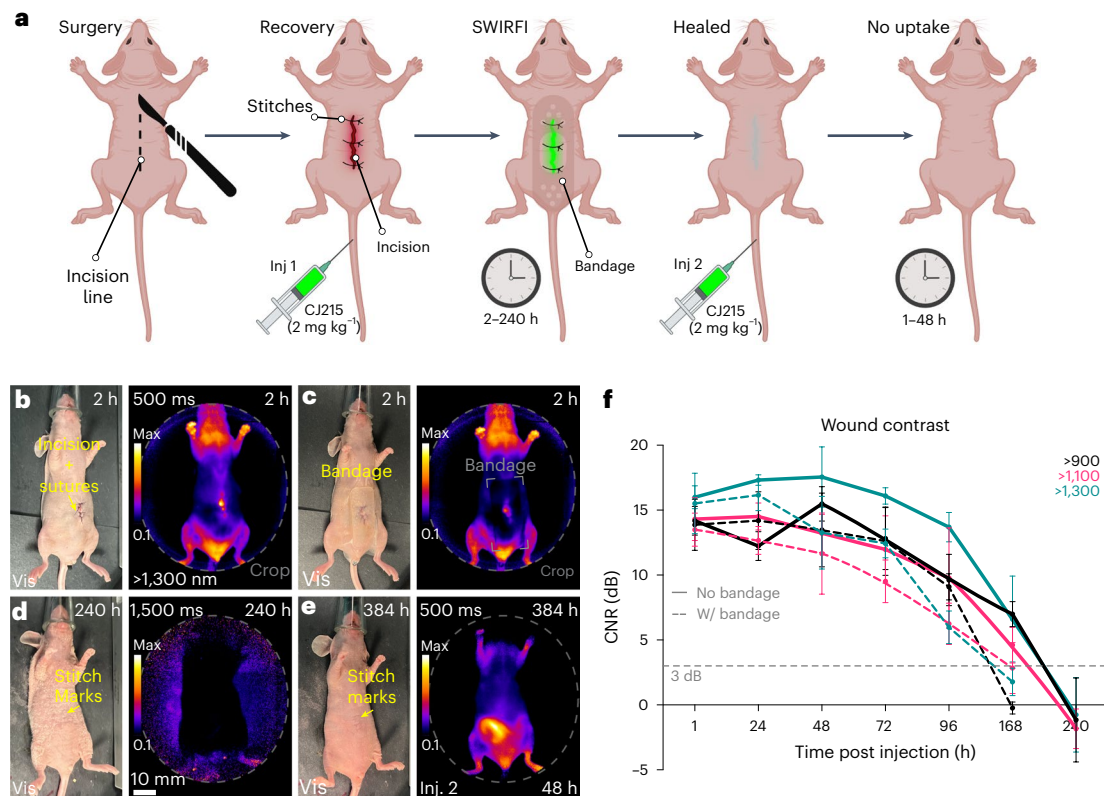


Fig. 8 | Non-invasive, non-contact and ambient-light-resistant wound monitoring through commercially available bandages via SWIRFI (>1,300 nm) and CJ215. **a**, Schematic representing the experimental protocol including the incision, suturing, injection and imaging timepoints. Mice received a second injection once the wound had healed and were then imaged every 24 h for 1–48 h post this injection. Created with Biorender.com. **b**, Representative visible-light and SWIRFI (>1,300 nm) images without a bandage at 2 h post surgery and CJ215 injection. **c**, The same mouse as in **a** but with a hydrogel bandage placed over the wound area. **d**, Representative images at 240 h post surgery and the first injection of CJ215, highlighting no remnant wound fluorescence (>1,300 nm). **e**, Representative images at 384 h post surgery and

48 h post the second injection of CJ215, highlighting no wound area uptake (wound has completely healed). **f**, Contrast quantification from all mice at all investigated wavelengths (>900, >1,100 and >1,300 nm cut-offs) with (solid lines) and without (dashed lines) bandage placement over wound area. Wound contrast peaks at 48 h post surgery and post injection, decreasing over time as the wound heals. Bandage application prevented wound delineation at 168 h. A 3 dB CNR threshold (grey dashed line) was utilized as before. In all cases, mean \pm s.d. are shown from $n = 4$ mice, with mice being measured immediately before and after bandage application. Video rate imaging (>900 nm) is shown in Supplementary Video 4, with all visible, >900, >1,100 and >1,300 nm images of all mice shown in Supplementary Figs. 39–42.

ratios in the mid 40 s (Fig. 4). Although not present in these single-site models, this highlights that CJ215 has the potential to delineate various organ metastases with high contrast for improved delineation. Importantly, these ratios were achieved by simply allowing CJ215 to clear from healthy tissue after a single systemic intravenous injection, with biodistribution data at 48 h post injection showing a similar trend, although with reduced tumour:muscle ratios (~ 9) (Supplementary Fig. 28). CJ215 cleared renally as highlighted by the retained kidney fluorescence, in stark comparison to other dyes or nanoparticle-based approaches where liver clearance can be a predominant factor (Fig. 4)^{35,58–60}. Select organs from these mice were assessed via histopathology (H&E staining), confirming tumour tissue from healthy organs and assessing additionally resected regions. All suspected tumour regions were confirmed to be tumourous via H&E staining.

During CT26 resection and necropsy, additional areas aside from the primary tumour demonstrated elevated organ:muscle ratios, (Fig. 5a,b). These regions were confirmed to be lymph node, uterine, ovarian, colon as well as the originally identified single-tumour site (Fig. 5c). IHC for CC3 (apoptosis marker) was performed on these tissues, highlighting their increased apoptotic levels (Fig. 5d). This also confirmed the highly apoptotic core seen at the centre of tumours, where CJ215 uptake had been brightest, (Fig. 3g and Supplementary Fig. 27). The exact cause of cellular damage and apoptosis in these regions is unclear; however, they were predominantly near the primary

tumour site and may have been compressed as it proliferated, causing reduced perfusion with cell stress and apoptosis.

Confirmation of the high tumour uptake, seen during SWIRFI screening, spurred us to present images in a way that would be most useful for FGS. Image presentation during surgery is an integral component of FGS when assessing novel systems and probes, and is ultimately where impact and utility of the approach are determined⁶¹. Sufficient SNR was always achieved with SWIRFI, but the main tumour delineation factor was concluded to be contrast (CNR), as expected (Fig. 2h,i). Here we present video rate images in a contrast mode where the user selects a non-tumourous background reference point (Fig. 6a). A custom script in ImageJ facilitated this across SWIRFI videos at >900 nm and achieved pixelwise image correction at a rate of 25.5 ms per image (Fig. 6b and Supplementary Video 3). The 3 dB threshold was found to be successful in highlighting tumour areas for all lines, fulfilling the Rose criterion^{49,50}. In addition, the conversion of images from a linear to a logarithmic scale counteracted the high tumour core uptake of CJ215, easing entire tumour delineation including the tumour margin (Fig. 6b CT26 model). This method enables binary tumour delineation on the fly for FGS and can be readily implemented by other researchers and for other probes. To further this method, we also assessed the ability of framewise corrections based on an average intensity projection of the video series. A slightly modified script enabled this, achieving image correction at a rate of 3.78 ms per frame versus 25.5 ms per frame for

CPU-based correction, providing a 6.75-fold reduction in processing time, potentially enabling near real-time display during surgery. Importantly, this method provided tumour delineation comparable to the pixelwise method (Supplementary Fig. 34). Graphics processing unit (GPU) implementation (outside the scope of this work, but possible with ImageJ) could further decrease image processing time and would probably be required to implement this method for real-time visualization (assuming image hand-off from memory to GPU is efficient) during FGS as opposed to during post processing with few ms acquisition times⁶².

With the success and high tumour localization of CJ215 in single-site tumour models, we next assessed its potential in a more challenging way. The SW1222 cell line is a human-derived, highly aggressive and metastatic tumour model, which spreads throughout the peritoneal space. Current clinical treatment includes surgical removal, where white-light visual inspection is utilized in a highly invasive surgery. This procedure comprises extracorporeal organ repositioning with peritoneal inspection and often fails to detect and remove all lesions. CJ215 was assessed in one such model where mice received SW1222 cells injected intraperitoneally (Fig. 7a)⁵⁵. Tumour growth was confirmed with luciferase, but SWIRFI and CJ215 (even at extended wavelengths, for example, >1300 nm) did not conclusively delineate tumours through the peritoneum and skin (which would not be the clinical approach anyway for FGS) (Fig. 7a and Supplementary Fig. 35). At 168 h post injection, SWIRFI resection was attempted, with tumours now being identified once the skin and peritoneum were removed as solid, necrotic tissue (probably dead), widely dispersed throughout the peritoneum and bound to the serosal surfaces of the intestines and spleen (Fig. 7b). NIRFI confirmed lower tumour uptake in the most necrotic tissues but did highlight large lesions spread around the spleen and pancreas, which could be readily delineated (Fig. 7b and Supplementary Fig. 36). Even though less successful than single-site models, CJ215 achieved tumour:muscle ratios of up to 10 within these tumours, with an uneven distribution across highly heterogeneous necrotic areas (Fig. 7c). Due to the rapid growth of these tumours and their widespread dispersion, they lacked viable vascular networks within necrotic tissue at the injection timepoint. The non-existent metabolic activity and poor blood delivery in dead and pervasively necrotic tissue hinders CJ215 delivery and therefore uptake in such lesions (Fig. 7b and Supplementary Fig. 36)⁶³. This is further highlighted by the high presence of disrupted blood vessels and necrotic tissue morphology in H&E staining of main tumours, versus the more viable and less necrotic peri-pancreatic tumours which presented higher tumour:muscle ratios.

Hair depilation during CT26 tumour imaging inadvertently inflicted minor wounds. We found serendipitously that these wounds showed high CJ215 uptake, with CJ215 clearing from them over time as they healed while remaining high in the adjacent tumour (Supplementary Fig. 37). This feature of CJ215 uptake is reminiscent of previous descriptions of tumours being wounds which do not heal⁶⁴. SWIR imaging is commonly used in industrial settings to detect, for example, liquids through substances that are opaque in the visible spectrum and therefore also to the human eye³⁹. We combined this aspect of SWIR sensors with SWIRFI to detect CJ215 through a variety of commercial bandages in phantoms (Supplementary Fig. 38). Hydrogel bandages, used in burn wound healing, were chosen to track wound healing in mice post a controlled incision (Fig. 8a,b and Supplementary Video 4)^{65,66}. Similar to tumour delineation, CNR could be inversely used to elucidate wound healing progression completely non-invasively after a single systemic injection of CJ215 (Fig. 8c). CNR increased up to 48 h post injection and then decreased as wounds healed in line with visible inspection (without bandages), with the >1,300 nm cut-off providing the highest CNR, albeit not at high video rate imaging (Fig. 8 and Supplementary Figs. 39–42). Having completely healed and following a second injection of CJ215, the wound area showed only minimal uptake, found to be

in line with non-injured skin (Supplementary Fig. 43). These mice also provided further biodistribution data of CJ215 in non-tumour-bearing conditions, confirming the renal clearance as seen at later timepoints and again the lack of uptake in other organs (Supplementary Fig. 43). This aspect of CJ215 and SWIRFI provides an objective, rapid (seconds) and quantitative solution in chronic wound monitoring with potential clinical applications in, for example, diabetic and burn wound victims⁶⁷. This will be especially useful where bandage removal may cause pain to patients or pose a risk to healing or of infection⁶⁵. On the basis of these experiments, a patient (even those not undergoing tumour resection) could receive a single injection of CJ215 upon surgery completion, with wound healing tracked for days during post-operative care. SWIRFI and CJ215 can readily visualize bandage-covered wounds under ambient lighting conditions, providing an additional application of clinical fluorescence imaging, not limited to only tumour resection.

Throughout this work, we have shown that CJ215 is highly tumour selective with excellent clearance from healthy organs. This clearance further aids tumour delineation and even enabled the detection of tumours on or close to non-affected organs. To further elucidate this mechanism, we computationally assessed the ability of CJ215 to non-covalently bind to both human and mouse albumin (HSA and MSA, respectively) (Extended Data Fig. 1). On the basis of our *in silico* investigation, we believe CJ215's favourable biodistribution and tumour retention is based on its high affinity to serum (GlideScore of -8.829 to HSA and -9.473 to MSA, indicating good binding). Due to this, CJ215 remains available for prolonged periods for uptake by tumours via the blood stream, especially when compared with ICG (GlideScore of -3.75 for HSA and -5.472 for MSA) (Extended Data Fig. 1). Cyanine dyes have been reported to bind to a moderately polar binding pocket between the IIA/IIB and IIIA subdomains of albumin^{68,69}. Our docking studies are in line with these findings, revealing multiple sites of ionic interaction between the carboxylic acid and sulfonate chains of CJ215 and the IIA/IIIA binding pocket of serum albumin. Importantly, for HSA CJ215 displayed far stronger interactions with serum than ICG. The key interaction residues in HSA are either partially conserved in the structure of MSA or are matched for properties, for example, R445 in HSA and K445 in MSA. We found that preliminary docking studies of CJ215 on MSA revealed similar binding poses and docking scores. However, this may be an artefact from using a predicted protein structure rather than an actual crystal structure. Note that these docking studies are based on non-covalent binding, and upon uptake into apoptotic cells, we believe that CJ215 is released from albumin and then resides within these cells, hence the correlation between CJ215 and apoptosis. However, further molecular biology work will be required to determine the exact mechanism, especially *in vivo*.

The *in silico* assessments are substantiated via CJ215's notable spectral changes when dissolved in FBS, HSA or blood compared with dextrose, further elucidating that *in vivo*, CJ215 is binding to serum and potentially other blood components. This is evidenced by the bathochromic shift in absorption peak of CJ215 in dextrose, HSA, FBS and blood (795, 805, 810 and 818 nm, respectively; Supplementary Figs. 2–4), with each solution presenting an increasingly convoluted environment and more components for CJ215 to bind to, more akin to *in vivo* settings. Importantly, following an initial red spectral shift, CJ215 underwent a slight blue shift over the course of days (-5 – 10 nm), potentially forming a covalent adduct with albumin and blood components, as shown for other carbocyanine dyes^{43,48}. In comparison to previous work, CJ215 contains a methoxy group on the cyclohexenyl ring at the centre of the heptamethine bridge as opposed to a chloride group along with some other subtle chemical differences⁴³. This methoxy group, and probably CJ215 as a whole, is less reactive than a carbocyanine dye with a chloride group at the same location, explaining the slow blue shift (days) in the presence of blood components.

On the basis of *in silico* assessments, *in vitro* and *in vivo* experimentation and biodistribution with renal clearance, we believe that CJ215

is predominantly binding to serum albumin (and perhaps other blood components) *in vivo*, which are then preferentially taken up by apoptotic and stressed cells including tumours and wound healing areas⁴⁸. This is further confirmed by our serum-free *in vitro* experiments and a biodistribution similarity to radiolabelled albumin, with protein catabolism by tumours and wound healing being a predominant driver of uptake^{43,70}. In terms of clinical translation, it is not yet clear what effect this serum binding will have in human patients. Importantly, the biological half-life of MSA is ~35 h, compared with ~500 h (~21 days) in humans^{71,72}. The MSA half-life can also be discerned by the reduced but still noticeable increase in CNR after 48 h, where high tumour retention combined with clearance both aid tumour visualization. It is possible that in humans, prolonged times between injection and surgery will be required to achieve CNR levels comparable to those seen preclinically. HSA binding is a known mechanism to deliver therapeutic agents to tumours and is also a known mechanism of delivery for, for example, paclitaxel, the efficacy of which can be improved by delivering in a nanoparticle format bound to HSA before injection^{73,74}. Binding to serum albumin (interestingly, at the same subdomains as tested here for CJ215) is also a known method for the delivery of ibuprofen, a widely utilized drug for non-tumour applications⁷⁵. Due to the need for good manufacturing practice grade production, toxicology and clinical trial costs, assessment of CJ215 in humans is far beyond the scope of this work. However, some preliminary assessments were made via normal and tumour tissue staining of flash-frozen human samples (tissue microarray) (Supplementary Fig. 45). As CJ215 does not provide antibody-based specificity and probably requires binding to albumin for its uptake, it (as expected) failed to conclusively distinguish tumour from normal tissue. We found that CJ215 readily bound to all tissues that survived the staining procedure itself. Importantly, the microarray does not recapitulate the dynamics of an *in vivo* setting (for example, albumin binding and delivery, blood flow, cell metabolism and clearance), hence conclusions should not be drawn from these data on the potential efficacy of CJ215 in human patients. In fact, this data further confirms our hypothesis of uptake mechanism (as all these factors are absent in this *ex vivo* staining experiment). Nevertheless, CJ215 successfully stained multiple human tissues, which could then be imaged with existing slide scanning systems.

One limitation of CJ215 is that based on our experimentation, CJ215 will probably not be of use in highly necrotic (dead) tumour tissue with poor vasculature as shown in the SW1222 model, similar to other agents. Based on the serum binding aspect of CJ215, it is clear that some form of functional vasculature is required for delivery, a known issue with necrotic tissue⁷⁶. However, surgery would most probably not be performed at this level of tumour burden. This is unlike the tested single-site tumour models, where CJ215 is readily delivered via the blood stream and vasculature, widely dispersed throughout the tumour and concentrated at highly apoptotic cores. Nevertheless, the SW1222 model did validate the ability of CJ215 to delineate peritoneal metastasis in multiple dispersed lesions. Due to the ability of CJ215 to highlight and be retained in apoptotic tissue, CJ215 may not be suitable for FGS in patients who have already received, for example, adjuvant chemotherapeutics which are known to cause off-target cell death⁷⁷. This would probably increase non-tumourous background uptake, potentially reducing tumour CNR or leading to false positives as seen in the CT26 model; however, uptake in the tumour could be increased as well to indicate tumour response, opening yet another avenue of application for CJ215. Conversely, due to the low uptake in healthy tissue and the established biodistribution seen here, CJ215 could be used to study these effects and organ protection provided by co-administered compounds. Fortunately, surgery is often the first treatment for most solid tumours, highlighting the suitability of CJ215 for tumour FGS within current surgical guidelines. While toxicology has not yet been confirmed, no adverse events were reported in any of the mice used herein, with all mice surviving the injections and main organs appearing

histologically normal. Repeated injections also caused no issue and as CJ215 is renally cleared, it may reduce potential liver toxicity.

In summary, CJ215 is a unique dye for tumour and wound monitoring through binding to mostly apoptotic cells, enabling delineation of various tumours in murine models (all tested models have been included, and we have yet to find a solid tumour model which CJ215 does not delineate) and quantitative wound monitoring. These aspects position CJ215 as a pan-cancer agent, with high tumour selectivity for multiple applications, reducing the often-limiting factor of FDA approval pipeline costs and bridging the 'valley' between preclinical and clinical translation. While promising, it is important to note that these results are yet to be replicated in larger mammals (for example, canine, porcine) and humans. It is likely that the increased size of tumours found in larger mammals will be of benefit for delineation with CJ215, as they will have increased levels of apoptosis. However, this cannot be tested in this work as upper tumour size is rightly limited for mice for both ethical and animal welfare reasons. Importantly, the logarithmic contrast mode images presented here will aid facilitation of boundary delineation in these larger tumours, unlike that seen in conventional linear representation, and may be of benefit for use with other dyes for FGS. Finally, CJ215 is a commercial product, facilitating rapid replication of these results and further investigation by any researcher with a suitable device (for example, IVIS). This is in stark comparison to the burden shouldered by academic labs where mass production of custom compounds is often unachievable and not a focus.

Methods

Spectral analysis

CJ215 (Proimaging) absorption spectra were determined after dissolving in either dextrose (5% Dextrose Inj. USP, 100/150 ml PAB, NDC 0264-1510-32, Braun Medical) or FBS at varying dye concentrations between 0.2 and 20 μ M using an ultraviolet-visible/NIR spectrometer (Jasco V-780, Jasco) in 100 μ l cuvettes using a dye free vehicle sample for correction, with readings displayed in optical density (OD). Extended SWIR tail emission was recorded using the same solutions on a 96-well optical plate (UV Half Area Plate, 3679, Corning) with a custom SWIR fluorescence spectrometer, as previously described⁴¹. Briefly, an 808 nm laser excitation source, inverted microscope (IX-71 microscope, Olympus) and $\times 20$ SWIR lens (Olympus) were used to collect spectra, with intensity artefacts corrected appropriately. Dextrose, FBS, HSA (H6914-20ML, MilliporeSigma) or defibrinated sheep's blood (R54004, ThermoFisher) were used to assess the spectral absorption and emission shift of CJ215 in solution over time, measured on a microplate (Corning UV-Transparent Microplates, CLS3679, MilliporeSigma) on an automated plate reader (SpectraMax ID5, Molecular Devices). Solutions were incubated in either 1.5 ml Eppendorfs or 15 ml tubes at 37 °C at 300 r.p.m. (Thermomixer R, Eppendorf).

In silico assessment

Plasma interaction of CJ215 and ICG was assessed via docking studies using the Schrodinger suite (release 2022-3) with the crystal structure of human serum albumin (HSA, pdb entry 1AO6) and the predicted structure (alpha fold, AF-P07724-F1) of MSA^{68,69,78-82}. Sequence homology of >72.37% was revealed via ALIGN⁸³. An initial docking study of CJ215 on MSA initially gave similar binding poses, albeit with lower scores. As such, the structures were aligned using the crystal structure of HSA as a template. The resulting new MSA structure (denoted MSA-2) was used subsequently for docking studies, which resulted in noted improvements to the glide scores obtained from flexible ligand docking. Previously suggested residues involved in plasma protein binding of cyanine dyes are either conserved or matched for their primary characteristic (for example, charge or hydrophobicity)^{84,85}. For the docking study, the cyanine backbone was limited to remain planar via torsion angle constriction along the polymethine backbone.

Electronic systems of cyanine dyes are unlikely to exist in their conjugated NIR-absorbing/emitting state if excessive torsion is applied along the backbone during flexible ligand docking⁸⁶. This is in contrast to the bathochromic shift observed in albumin-containing solutions. Of note, certain approximations must be made when docking cyanine dyes via the Schrodinger suite; for example, the delocalized nature of the charge across the polymethine backbone cannot be modelled accurately and is instead represented in a localized charge on one of the nitrogen centres. This aspect may result in attractive or repulsive forces which may actually be weaker in vitro/in vivo.

In vitro assessment

4T1 (ATCC, CRL-2539) cells were cultured in RPMI media (supplemented with Pen-Strep and FBS) until confluent in 6-well plastic poly-D-lysine coated plates with an embedded glass coverslip (P06G-1.5-10-F, MatTek). In these conditions, 4T1 cells formed a mix of single cells and spheroid aggregations. Cells were washed once with fresh medium, then incubated (37 °C, 5% CO₂) with CJ215 (suspended in cell culture medium) for 3 h at a concentration of 0.645 mM. Stock DAPI solution (1 µl; 62248, ThermoFisher) was added to each well at 2 h and 40 min into CJ215 incubation. At 3 h, well media were aspirated, cells washed once with fresh medium and then 1 ml of medium was added to each well. Point scanning confocal microscopy was then performed (STELLARIS 8, Leica) within an hour, recording various images (stacks, videos) with appropriate DAPI, CJ215 and polarized white-light settings. Images were imported into ImageJ, split by colour with Gaussian blur (sigma=1) applied to DAPI and CJ215 channels, followed by contrast adjustment for easier visualization before remerging the channels. For multidye staining, 4T1 cells were grown in the same manner as before. CJ215 was once again added at a 0.645 mM concentration for a 3 h incubation period. At 1 h into this incubation period, diluted LysoTracker Red DND-99 (CN: L7528) dye was added directly to cell media to reach a concentration of 50 nM. After 2 h and 50 min of incubation, Hoechst 33342 solution (CN: 62249) and CellMask plasma membrane stain (CN: C37608) were added directly to cell media to reach a concentration of 0.001 g l⁻¹ and 1x solution, respectively. Foil was placed to cover cells and cells were incubated for 5–10 min at 37 °C. Cells were washed with RPMI media 2x and left in media without fluorescent dye. Confocal microscopy was performed immediately at appropriate settings. Images and Z-stack timeseries with all four fluorescent dyes as well as brightfield images were acquired.

Active transport was assessed also using 4T1 cells incubated in pre-coated plastic 6-well plates (no glass coverslip). Cells were washed once and then placed into either a fridge or an incubator for 10 min before incubation with CJ215 as performed for confocal imaging. CJ215 uptake was assessed using the 700 and 800 channels on an Odyssey CLx infrared imaging system, with image analysis, consisting of determining the mean fluorescence within each well (Fiji/ImageJ)⁸⁷, performed on .tiff images. HT1080 (ATCC, CCL-121) cells (75,000 cells per well) were seeded on a 24-well plate with 500 µl of cell medium (DMEM, with Pen-Strep and 10% FBS). After 24 h, the cells had attached to the plate surface and staurosporine was added to the wells at a final concentration of 2 µM staurosporine. The cells were incubated with staurosporine for 18 h. CJ215 stock solution (5 µl, 0.5 mg ml⁻¹) was mixed with 1.2 ml media and 50 µl dye-media mix was added to each well. Dye was incubated with the cells for an additional 6 h, then cells were washed with PBS once. The plate was imaged and quantified as before (Odyssey CLx and Fiji/ImageJ). Serum-free and serum uptake of CJ215 was assessed with 4T1 cells plated on 6-well plates as before. Cells were starved in serum-free conditions (cell medium without FBS) for 3 h before addition of and incubation with CJ215, also as before. Cells were washed once with respective media, fixed and imaged in 1 ml of formaldehyde solution (4%, microscopy grade, 1.00496.5000, Sigma-Aldrich) and imaged as before (Odyssey CLx). Formaldehyde stability of CJ215 was assessed

with the same cells stored at 4 °C for up to 9 days post fixation, again imaged as before.

In vivo experimentation

Single-tumour model sites were generated with multiple cells, mouse lines and sexes. In brief, 4T1 cells (3.0 × 10⁵) suspended in 30 µl of Matrigel were injected into the mammary pad of female FoxN1tm mice. PC3 cells (5 × 10⁶) expressing human prostate-specific membrane antigen (PC3-PSMA) suspended in 50 µl of PBS were subcutaneously injected into the flank of male NOD.Cg-Prkdcscid/J mice. HT1080 cells (5 × 10⁶) suspended in 100 µl of 50:50 Matrigel and PBS were subcutaneously injected into the flank, at the top of the leg in female FoxN1tm mice. CT26 cells (2 × 10⁶) suspended in PBS were subcutaneously injected into the flank of female BALB/cAnN mice. Mice were utilized at various ages, with tumours allowed to proliferate until tumours of various sizes, approximately >50 mm³, could be visually determined. For CJ215 biodistribution assessments at a 48 h timepoint, 1.5 × 10⁵ 4T1-Luc cells suspended in PBS were injected into the mammary fat pad of female BALB/cAnN mice. SW1222 cells (5.0 × 10⁶) expressing luciferase suspended in 100 µl of cell medium were intraperitoneally injected into female FoxN1tm mice sporadically forming tumour lesions and assessed using luciferin. Female FoxN1tm mice (bearing no tumours) were also used for wound healing experiments. For ICG experiments, 3.0 × 10⁵ 4T1 cells suspended in 30 µl of Matrigel were injected into the mammary pad of female FoxN1tm mice.

In all cases, mice received a 2 mg kg⁻¹ intravenous injection of CJ215 suspended in clinical-grade dextrose. Upon receipt of CJ215, it was suspended in dextrose, aliquoted into glass dram vials and lyophilised for storage at -20 °C. Injection solutions were prepared within 1 h before administration, with solutions appearing dark green. The dye did not form any noticeable clumps, could be readily resuspended in dextrose by simply using a pipette and animal injections went smoothly. CJ215 was not handled in any overly restrictive or particular manner, and no adverse event was noticed post dye injection. For ICG experimentation, mice received a 2 mg kg⁻¹ intravenous injection of ICG (I01250, Pfaltz & Bauer) dissolved in clinical-grade dextrose as performed for CJ215 imaging. All mouse handling, experimentation, imaging and housing was performed according to National Institutes of Health guidelines and via approved Institutional Animal Care and Use Committee protocols at Memorial Sloan Kettering Cancer Center. Mice received food and water ad libitum under a 12 h on/off light cycle, with 5 mice per cage with food. FoxN1tm mice used in tumour experiments were fed either a solid amoxicillin or sulfatrim-based diet to counteract skin infections. SW1222 and wound healing mice were placed on a low-autofluorescence diet to counteract observed intestinal signals, with wound healing mice receiving sulfatrim water to counteract skin infections. Surgery was performed on mice in line with preapproved protocols, with mice having anaesthesia induced at 3% v/v, followed by maintenance at 1–2% v/v in oxygen and placement on a heating pad. Before surgery, the mice subcutaneously received buprenorphine (0.5 mg kg⁻¹) and meloxicam (2 mg kg⁻¹) with bupivacaine (0.1 cc) administered at the incision site for numbing. The surgical field was cleaned for surgery using sets of alternating scrubs (alternating either povidine-iodine (betadine), chlorhexidine or 70% isopropyl alcohol). All surgical instruments were sterilized by steam sterilization and using a glass bead sterilizer between animals. A scalpel was used to create a 1 cm incision, with wound sealing performed with monofilament absorbable suture (monocryl). Mice were monitored post recovery every 24 h and received meloxicam (2 mg kg⁻¹) subcutaneously for up to 72 h post surgery.

Tumour resection was performed only on mice that had been euthanized via CO₂ inhalation, in line with approved protocols. Following this, the tumour was resected under white-light visualization, with resection confirmed using SWIRFI. Necropsy biodistribution was assessed by isolating the following organs: tumour or wound site, liver, kidneys, lungs, brain, spleen, pancreas, stomach, small and large intestines, skin, bone, muscle and heart.

SWIRFI and NIRFI

Ambient-light-resistant SWIRFI was performed as previously described⁴¹. In brief, a hyperspectral SWIR system (IR-VIVO, Photon etc.) equipped with an 808 nm laser ($\sim 300 \text{ mW cm}^{-2}$) for dye excitation, a 940 nm LED for SWIR white light (reflectance imaging) and an RGB LED was used for SWIRFI. The ambient lighting LED was on for all SWIRFI images presented throughout this manuscript. Extended emission imaging was achieved using suitable long-pass optical filters (Thorlabs) mounted in front of the lens of the system in a custom mount. Exposure times ranged from 1–1,500 ms with data stored in a .h5 format. Images were converted to tiff files with corrections then performed in Fiji/ImageJ as before, including dark noise subtraction, outlier removal and cropping⁴¹. Defined ROIs were used to assess brightness, SNR and CNR, also as previously described⁴¹. NIRFI for biodistribution was performed using an IVIS Spectrum (PerkinElmer) with ICG-based filter sets (745 nm excitation and 840 nm emission) at exposure times of 5–20 s, high lamp, f# of 1 and small binning. Organ quantification was performed in ImageJ/Fiji with ROIs drawn across each organ in the raw luminescent tiff file exported from the IVIS system. This system was also used for luciferase imaging of SW1222 mice in bioluminescence mode. For all live animal imaging, mice were anaesthetized using isoflurane inhalation at an induction of 3% v/v and maintenance of 1–2% v/v in O_2 , and were placed on a heating pad during imaging.

Histological assessment

Paraffin-embedded organs (tumour or wound, liver, kidney, spleen and muscle) were prepared as previously described to generate either 5- μm -thick unstained or H&E-stained (Leica Autostainer, ST5010) slides⁴¹. H&E slides were imaged using an automated slide scanner at $\times 20$ magnification (0.8 NA, 3DHitech), with representative images shown at $\times 20$ (SlideViewer v.2.5, 3DHitech). Immunohistochemistry for CC3 was performed on paraffin sections using a Leica Bond RX automated stainer. After heat-induced epitope retrieval in a pH 6.0 buffer, anti-CC3 antibody (Cell Signaling, 9661) was applied at a concentration of 1:250, followed by a polymer detection reagent kit according to manufacturer instructions (DS9800, Novocastra Bond Polymer Refine Detection, Leica Biosystems). The chromogen indicating positive immunoreactivity was 3,3-diaminobenzidine tetrachloride (DAB), and sections were counterstained with haematoxylin. CC3 IHC images were acquired on an Olympus VS200 slide scanner and VS200 ASW 3.4.1 software (Evident Scientific) using a $\times 20/0.80\text{NA}$ objective to generate whole-slide images with a pixel size of $0.2738 \mu\text{m}$. CC3 images are presented at various magnifications after visualization in QuPath (v.0.4.4) and image export to Fiji/ImageJ2 (v.2.14.0/1.54g)^{87,88}. Select H&E and CC3 whole-slide images were examined by a board-certified veterinary pathologist (S.M.).

Data analysis

Cellular co-localization analysis was performed using available plugins in Fiji/ImageJ2. Images were cropped to frame selected cells, channels split and subsequent channels underwent background subtraction (rolling ball of 50) followed by Gaussian blur ($\sigma=1$). Z-stack timeseries were split into a selected slice base for analysis. Channels were merged with all dyes, all dyes and brightfield, or CJ215 with either CellMask plasma membrane, nucleus, or lysosomal dye. Three-dimensional (3D) point spread functions for each image or z-stack series were computed using the Diffraction PSF 3D plugin⁸⁹. Individual dye channels were then deconvolved using the Iterative Deconvolve 3D ImageJ plugin⁹⁰. Co-localization analysis was performed using the Coloc 2 ImageJ plugin comparing the deconvolved CJ215 image to each of the deconvolved CellMask plasma membrane channel, deconvolved Hoechst 33342 nucleus channel and deconvolved LysoTracker Red DND-99 channel. Deconvolution and co-localization analyses were conducted for multiple consecutive frames when feasible, with the Pearson's R value for co-localization reported.

Image processing and quantification was performed in ImageJ/Fiji with results saved in Excel files (Excel for Mac, v.16.57, Microsoft). SNR and CNR values were calculated in Excel, with graphing with various statistical analyses as listed performed in GraphPad Prism (Prism 10 for MacOS). A custom script (macro) was developed in ImageJ/Fiji for both pixelwise and framewise/stack correction of SWIRFI images on the basis of a user-defined ROI. The script calculated the mean and s.d. of this ROI for all frames in a video image and used the CNR formula commonly utilized to present images in 'contrast mode'.

Wound healing assessment

Assessed bandages in phantom imaging included hydrocolloid gel (990443, $33 \times 53 \text{ mm}$, Walgreens), hydrogel (973181, $44.5 \times 73 \text{ mm}$ or $25 \times 56 \text{ mm}$, Walgreens), transparent ($60 \times 70 \text{ mm}$, TEGADERM, Nexcare, 3M, 666368, Walgreens) and liquid spray (on saran wrap, 202297, Walgreens). Hydrogel bandages were applied to mice only during imaging, with each mouse receiving a new bandage at every imaging time point, and the bandage being removed before removing the mouse from the imaging setup.

Human tissue staining

A flash-frozen human tissue microarray (T6235700-5, Frozen Tissue Array, amsbio) was used to assess the ability of CJ215 to stain 14 various human tumours and representative normal tissue samples ranging from uterine to brain tissue samples. Upon delivery, slides were stored at $-80 \text{ }^\circ\text{C}$ and defrosted before use. For H&E staining, a slide was baked at $60 \text{ }^\circ\text{C}$ for 1 h, followed by H&E staining as previously described. Consecutive slides were then defrosted and a $200 \mu\text{l}$ drop of CJ215 ($85 \mu\text{M}$ concentration) was added to each slide. A strip of parafilm large enough to cover all cores was then placed over the drop and onto the array, ensuring that all tissue cores were covered with dye solution. The slide was then left to incubate with the dye for 1 h in a dark humid box, followed by washing with dextrose (dipping two times into a 45 ml well). Immediately following this, $200 \mu\text{l}$ of Mowiol was added to the slide, followed by careful mounting with a glass coverslip and drying ($\sim 30 \text{ min}$). The slide was then imaged using the same automated slide scanner (3DHitech) as previously utilized but with the Cy7-750 channel (15% excitation intensity, 20 ms exposure time, 0 gain) and visualized as before (SlideViewer v.2.5, 3DHitech).

Reporting summary

Further information on research design is available in the Nature Portfolio Reporting Summary linked to this article.

Data availability

The raw and analysed datasets generated during the study are available for research purposes from the corresponding author on reasonable request. Source data are provided with this paper.

Code availability

The code required to generate the CNR images via framewise or pixelwise methods is included in the Supplementary Information. All code to process the images in ImageJ is readily available via plugins.

References

- Liu, J. T. & Sanai, N. Trends and challenges for the clinical adoption of fluorescence-guided surgery. *J. Nucl. Med.* **60**, 756–757 (2019).
- Pogue, B. W. Perspective on the optics of medical imaging. *J. Biomed. Opt.* **28**, 121208–121208 (2023).
- Sutton, P. A. et al. Fluorescence-guided surgery: comprehensive review. *BJS Open* **7**, zrad049 (2023).
- Teng, C. W. et al. Second window ICG predicts gross-total resection and progression-free survival during brain metastasis surgery. *J. Neurosurg.* **135**, 1026–1035 (2021).

5. Li, M. et al. 800CW dye and 89Zr dual-labeled antibody for the PET/NIRF/Cerenkov multi-modality imaging of ICAM-1 (CD54) in pancreatic cancer. *J. Nucl. Med.* **60**, 331 (2019).
6. Tsuboi, S. & Jin, T. Shortwave-infrared (SWIR) fluorescence molecular imaging using indocyanine green–antibody conjugates for the optical diagnostics of cancerous tumours. *RSC Adv.* **10**, 28171–28179 (2020).
7. Hollandsworth, H. M., Turner, M. A., Hoffman, R. M. & Bouvet, M. A review of tumor-specific fluorescence-guided surgery for colorectal cancer. *Surg. Oncol.* **36**, 84–90 (2021).
8. Gao, R. W. et al. Safety of panitumumab-IRDye800CW and cetuximab-IRDye800CW for fluorescence-guided surgical navigation in head and neck cancers. *Theranostics* **8**, 2488–2495 (2018).
9. Gutowski, M. et al. SGM-101: an innovative near-infrared dye–antibody conjugate that targets CEA for fluorescence-guided surgery. *Surg. Oncol.* **26**, 153–162 (2017).
10. Nunn, A. D. The cost of developing imaging agents for routine clinical use. *Invest. Radiol.* **41**, 206–212 (2006).
11. Paul, S. M. et al. How to improve R&D productivity: the pharmaceutical industry’s grand challenge. *Nat. Rev. Drug Discov.* **9**, 203–214 (2010).
12. Nagaya, T., Nakamura, Y. A., Choyke, P. L. & Kobayashi, H. Fluorescence-guided surgery. *Front. Oncol.* **7**, 314 (2017).
13. Smith, T. et al. The cost of OR time is \$46.04 per minute. *J. Orthop. Business* **2**, 10–13 (2022).
14. Kinch, M. S. & Woodard, P. K. Analysis of FDA-approved imaging agents. *Drug Discov. Today* **22**, 1077–1083 (2017).
15. Crawford, T. et al. pHILIP ICG for delineation of tumors and blood flow during fluorescence-guided surgery. *Sci. Rep.* **10**, 18356 (2020).
16. Kaynak, A. et al. Phosphatidylserine: the unique dual-role biomarker for cancer imaging and therapy. *Cancers* **14**, 2536 (2022).
17. Fouad, Y. A. & Aanei, C. Revisiting the hallmarks of cancer. *Am. J. Cancer Res.* **7**, 1016–1036 (2017).
18. Hanahan, D. & Weinberg, R. A. Hallmarks of cancer: the next generation. *Cell* **144**, 646–674 (2011).
19. Kobayashi, H., Watanabe, R. & Choyke, P. L. Improving conventional enhanced permeability and retention (EPR) effects; what is the appropriate target? *Theranostics* **4**, 81–89 (2014).
20. Jensen, R. L. Brain tumor hypoxia: tumorigenesis, angiogenesis, imaging, pseudoprogression, and as a therapeutic target. *J. Neurooncol.* **92**, 317–335 (2009).
21. Pfeffer, C. M. & Singh, A. T. Apoptosis: a target for anticancer therapy. *Int. J. Mol. Sci.* **19**, 448 (2018).
22. Barth, N. D. et al. A fluorogenic cyclic peptide for imaging and quantification of drug-induced apoptosis. *Nat. Commun.* **11**, 4027 (2020).
23. Widen, J. C. et al. AND-gate contrast agents for enhanced fluorescence-guided surgery. *Nat. Biomed. Eng.* **5**, 264–277 (2021).
24. Cho, H. et al. Polymeric micelles for apoptosis-targeted optical imaging of cancer and intraoperative surgical guidance. *PLoS ONE* **9**, e89968 (2014).
25. Shi, X. et al. Near-infrared window II fluorescence image-guided surgery of high-grade gliomas prolongs the progression-free survival of patients. *IEEE Trans. Biomed. Eng.* **69**, 1889–1900 (2021).
26. Tran-Guyon, J., Guyon, V. & Scherninski, F. European Patent Office EP4149925A1 (Google Patents, 2023).
27. Pulaski, B. A. & Ostrand-Rosenberg, S. Mouse 4T1 breast tumor model. *Curr. Protoc. Immunol.* <https://doi.org/10.1002/0471142735.im2002s39> (2000).
28. Flores, O. et al. PSMA-targeted theranostic nanocarrier for prostate cancer. *Theranostics* **7**, 2477–2494 (2017).
29. Miwa, S. et al. Inhibition of spontaneous and experimental lung metastasis of soft-tissue sarcoma by tumor-targeting *Salmonella typhimurium* A1-R. *Oncotarget* **5**, 12849–12861 (2014).
30. Richman, P. I. & Bodmer, W. F. Control of differentiation in human colorectal carcinoma cell lines: epithelial–mesenchymal interactions. *J. Pathol.* **156**, 197–211 (1988).
31. Czajka, M. L. & Pfeifer, C. *Breast Cancer Surgery* (StatPearls Publishing, 2020).
32. Kim, E. H. & Bullock, A. D. Surgical management for prostate cancer. *Mo. Med.* **115**, 142–145 (2018).
33. Augsburger, D. et al. Current diagnostics and treatment of fibrosarcoma – perspectives for future therapeutic targets and strategies. *Oncotarget* **8**, 104638–104653 (2017).
34. Matsuda, T. et al. Recent updates in the surgical treatment of colorectal cancer. *Ann. Gastroenterol. Surg.* **2**, 129–136 (2018).
35. Glehen, O. et al. Cytoreductive surgery combined with perioperative intraperitoneal chemotherapy for the management of peritoneal carcinomatosis from colorectal cancer: a multi-institutional study. *J. Clin. Oncol.* **22**, 3284–3292 (2004).
36. Riwaldt, S. et al. Role of apoptosis in wound healing and apoptosis alterations in microgravity. *Front. Bioeng. Biotechnol.* **9**, 679650 (2021).
37. Greenhalgh, D. G. The role of apoptosis in wound healing. *Int. J. Biochem. Cell Biol.* **30**, 1019–1030 (1998).
38. Fogarty, C. E. & Bergmann, A. Killers creating new life: caspases drive apoptosis-induced proliferation in tissue repair and disease. *Cell Death Differ.* **24**, 1390–1400 (2017).
39. Belsky, J. Short wave infrared enhances machine vision: the machine vision professional gains a new tool with SWIR. *Quality* **52**, 16VS (2013).
40. Carr, J. A. et al. Shortwave infrared fluorescence imaging with the clinically approved near-infrared dye indocyanine green. *Proc. Natl Acad. Sci. USA* **115**, 4465–4470 (2018).
41. Mc Larney, B. E. et al. Ambient light resistant shortwave infrared fluorescence imaging for preclinical tumor delineation via the pH low-insertion peptide conjugated to indocyanine green. *J. Nucl. Med.* **64**, 1647–1653 (2023).
42. Cosco, E. D., Lim, I. & Sletten, E. M. Photophysical properties of indocyanine green in the shortwave infrared region. *ChemPhotoChem* **5**, 727–734 (2021).
43. Usama, S. M. et al. Role of albumin in accumulation and persistence of tumor-seeking cyanine dyes. *Bioconjug. Chem.* **31**, 248–259 (2020).
44. Carr, J. A. et al. Absorption by water increases fluorescence image contrast of biological tissue in the shortwave infrared. *Proc. Natl Acad. Sci. USA* **115**, 9080–9085 (2018).
45. Jacques, S. L. Optical properties of biological tissues: a review. *Phys. Med. Biol.* **58**, R37–R61 (2013).
46. Madani, F., Lindberg, S., Langel, Ü., Futaki, S. & Gräslund, A. Mechanisms of cellular uptake of cell-penetrating peptides. *J. Biophys.* **2011**, 414729 (2011).
47. Yuste, V. J. et al. The prevention of the staurosporine-induced apoptosis by Bcl-XL, but not by Bcl-2 or caspase inhibitors, allows the extensive differentiation of human neuroblastoma cells. *J. Neurochem.* **80**, 126–139 (2002).
48. Usama, S. M. & Burgess, K. Hows and whys of tumor-seeking dyes. *Acc. Chem. Res.* **54**, 2121–2131 (2021).
49. Dieckens, D., Lavalaye, J., Romijn, L. & Habraken, J. Contrast-noise-ratio (CNR) analysis and optimisation of breast-specific gamma imaging (BSGI) acquisition protocols. *EJNMMI Res.* **3**, 21 (2013).
50. Cherry, S. R., Sorenson, J. A. & Phelps, M. E. *Physics in Nuclear Medicine* 3rd edn (Saunders, 2003).
51. Zhu, S. et al. Repurposing cyanine NIR-I dyes accelerates clinical translation of near-infrared-II (NIR-II) bioimaging. *Adv. Mater.* **30**, 1802546 (2018).

52. Gown, A. M. & Willingham, M. C. Improved detection of apoptotic cells in archival paraffin sections: immunohistochemistry using antibodies to cleaved caspase 3. *J. Histochem. Cytochem.* **50**, 449–454 (2002).
53. Sabapathy, V., Mentam, J., Jacob, P. M. & Kumar, S. Noninvasive optical imaging and in vivo cell tracking of indocyanine green labeled human stem cells transplanted at superficial or in-depth tissue of SCID mice. *Stem Cells Int.* **2015**, 606415 (2015).
54. Klaver, Y. L., Lemmens, V. E., Nienhuijs, S. W., Luyer, M. D. & de Hingh, I. H. Peritoneal carcinomatosis of colorectal origin: incidence, prognosis and treatment options. *World J. Gastroenterol.* **18**, 5489–5494 (2012).
55. Chandler, C. S. et al. Intraperitoneal pretargeted radioimmunotherapy for colorectal peritoneal carcinomatosis. *Mol. Cancer Ther.* **21**, 125–137 (2022).
56. Ide, T. et al. LED light characteristics for surgical shadowless lamps and surgical loupes. *Plast. Reconstr. Surg. Glob. Open* **3**, e562 (2015).
57. Zhu, J., Li, H., Conti, P., Shi, X. & Chen, K. 64Cu-Labeled polyethyleneimine-coated manganese oxide nanoparticles for targeted tumor PET/MR imaging. *Soc. Nuclear Med.* **57** (Suppl. 2), 1187 (2016).
58. Wang, F. et al. High-precision tumor resection down to few-cell level guided by NIR-IIb molecular fluorescence imaging. *Proc. Natl Acad. Sci. USA* **119**, e212311119 (2022).
59. Lim, I. et al. Shortwave infrared fluorofluorophores for multicolor in vivo imaging. *Angew. Chem.* **135**, e202215200 (2023).
60. Bandi, V. G. et al. Targeted multicolor in vivo imaging over 1,000 nm enabled by nonamethine cyanines. *Nat. Methods* **19**, 353–358 (2022).
61. Elliott, J. T. et al. Review of fluorescence guided surgery visualization and overlay techniques. *Biomed. Opt. Express* **6**, 3765–3782 (2015).
62. Haase, R. et al. CLIJ: GPU-accelerated image processing for everyone. *Nat. Methods* **17**, 5–6 (2020).
63. Liu, Z.-g & Jiao, D. Necroptosis, tumor necrosis and tumorigenesis. *Cell Stress* **4**, 1–8 (2020).
64. Dvorak, H. F. Tumors: wounds that do not heal—redux. *Cancer Immunol. Res.* **3**, 1–11 (2015).
65. Brumberg, V., Astrelina, T., Malivanova, T. & Samoilov, A. Modern wound dressings: hydrogel dressings. *Biomedicines* **9**, 1235 (2021).
66. Stoica, A. E., Chircov, C. & Grumezescu, A. M. Hydrogel dressings for the treatment of burn wounds: an up-to-date overview. *Materials* **13**, 2853 (2020).
67. Kenworthy, P. et al. Monitoring wound healing in minor burns—a novel approach. *Burns* **44**, 70–76 (2018).
68. Jumper, J. et al. Highly accurate protein structure prediction with AlphaFold. *Nature* **596**, 583–589 (2021).
69. Sugio, S., Kashima, A., Mochizuki, S., Noda, M. & Kobayashi, K. Crystal structure of human serum albumin at 2.5 Å resolution. *Protein Eng.* **12**, 439–446 (1999).
70. Stehle, G. et al. Plasma protein (albumin) catabolism by the tumor itself—implications for tumor metabolism and the genesis of cachexia. *Crit. Rev. Oncol. Hematol.* **26**, 77–100 (1997).
71. Chaudhury, C. et al. The major histocompatibility complex-related Fc receptor for IgG (FcRn) binds albumin and prolongs its lifespan. *J. Exp. Med.* **197**, 315–322 (2003).
72. Peters, T. Jr Serum albumin. *Adv. Protein Chem.* **37**, 161–245 (1985).
73. Awosika, A. O, Farrar, M.C. & Jacobs T. F. Paclitaxel (StatPearls Publishing, 2023); <https://europepmc.org/article/nbk/nbk536917>
74. Tian, Z. & Yao, W. Albumin-bound paclitaxel: worthy of further study in sarcomas. *Front. Oncol.* **12**, 815900 (2022).
75. Ploch-Jankowska, A. & Pentak, D. A comprehensive spectroscopic analysis of the ibuprofen binding with human serum albumin, part I. *Pharmaceuticals* **13**, 205 (2020).
76. Yee, P. P. & Li, W. Tumor necrosis: a synergistic consequence of metabolic stress and inflammation. *Bioessays* **43**, 2100029 (2021).
77. Zeien, J. et al. Clinical implications of chemotherapeutic agent organ toxicity on perioperative care. *Biomed. Pharmacother.* **146**, 112503 (2022).
78. Friesner, R. A. et al. Glide: a new approach for rapid, accurate docking and scoring. 1. Method and assessment of docking accuracy. *J. Med. Chem.* **47**, 1739–1749 (2004).
79. Friesner, R. A. et al. Extra precision glide: docking and scoring incorporating a model of hydrophobic enclosure for protein–ligand complexes. *J. Med. Chem.* **49**, 6177–6196 (2006).
80. Varadi, M. et al. AlphaFold Protein Structure Database: massively expanding the structural coverage of protein–sequence space with high-accuracy models. *Nucleic Acids Res.* **50**, D439–D444 (2022).
81. Varadi, M. et al. AlphaFold Protein Structure Database in 2024: providing structure coverage for over 214 million protein sequences. *Nucleic Acids Res.* **52**, D368–D375 (2024).
82. Berman, H. M. et al. The protein data bank. *Nucleic Acids Res.* **28**, 235–242 (2000).
83. Bateman, A. et al. UniProt: the universal protein knowledgebase in 2023. *Nucleic Acids Res.* **51**, D523–D531 (2023).
84. Kostyukov, A. et al. Molecular docking simulation and fluorescence lifetime characteristics of nir cyanine dye complexes with albumin. In *IOP Conference Series: Materials Science and Engineering* Vol. 848, 012040 (IOP Publishing, 2020).
85. Tian, R. et al. Albumin-chaperoned cyanine dye yields superbright NIR-II fluorophore with enhanced pharmacokinetics. *Sci. Adv.* **5**, eaaw0672 (2019).
86. Le Guennic, B. & Jacquemin, D. Taking up the cyanine challenge with quantum tools. *Acc. Chem. Res.* **48**, 530–537 (2015).
87. Schindelin, J. et al. Fiji: an open-source platform for biological-image analysis. *Nat. Methods* **9**, 676–682 (2012).
88. Bankhead, P. et al. QuPath: open source software for digital pathology image analysis. *Sci. Rep.* **7**, 16878 (2017).
89. Dougherty, R. Extensions of DAMAS and benefits and limitations of deconvolution in beamforming. In *11th AIAA/CEAS Aeroacoustics Conference* 2961 (AIAA, 2005).
90. Landmann, L. Deconvolution improves colocalization analysis of multiple fluorochromes in 3D confocal data sets more than filtering techniques. *J. Microsc.* **208**, 134–147 (2002).

Acknowledgements

We thank S. Urbain and F. Scherninski from Proimaging (Paris, France) along with J. Tran-Guyon and V. Guyon from Laboratoires Synth-Innove (Paris, France) for helpful advice, discussions and for providing CJ215 for this investigation (CJ215 was a gift from Proimaging which did not sponsor this research other than providing CJ215); the small-animal imaging core at MSKCC for assistance as well as RARC at MSKCC for advice on animal experiments and excellent animal assistance, especially A. Ritter and E. Soto-Lemus; N. Fan, B. Shrestha and W. Kang of the Molecular Cytology Core Facility at MSKCC and I. Miranda of the Laboratory of Comparative Pathology at MSKCC; E. Chan, E. Rosiek and Y. Romin of the Molecular Cytology core at MSKCC for microscopy assistance. Support for this work was provided by the the National Science Foundation CAREER Award (1752506, D.A.H.), the NCI (R01-CA-257811, J.G., R01-CA215719, D.A.H. and Cancer Center Support Grant P30-CA008748, Selwyn Vickers/MSKCC), NIBIB (R56 EB030512, J.G., R01-EBO33651, D.A.H.; R00-EBO33580, M.K.), the Department of Defense Congressionally Directed Medical Research Program (W81XWH-22-1-0563, D.A.H.), the Ara Parseghian Medical Research Fund (D.A.H.), the American Cancer Society Research Scholar Grant (GC230452, D.A.H.), the Louis and Rachel Rudin Foundation (D.A.H.), MSK's Cycle for Survival's Equinox Innovation Award in Rare Cancers (D.A.H.), the Experimental Therapeutics Center of MSKCC

(D.A.H. and J.G.), Mr. William H. Goodwin and Mrs. Alice Goodwin and the Commonwealth Foundation for Cancer Research (D.A.H.) and the Vince Lombardi Cancer Foundation (J.G.). This work was partially funded by Memorial Sloan Kettering Cancer Center's Technology Development Funding Program, flexTDF (D.V.).

Author contributions

B.E.M.L. conceived, designed and performed the experiments, and designed the analysis pipelines and CNR code. A.Y.S. designed and performed Sta and zVAD experiments. E.A. designed and performed in vivo experiments. B.E.M.L. and C.H. performed in vitro assessment and microscopy. B.E.M.L., D.G. and M.K. performed spectral characterization. R.M.E. performed the in silico serum docking assessment. N.A. and D.V. generated and assisted with metastatic modelling. S.M. performed pathology analysis and staining. N.M., E.I., N.B.P. and M.S. generated various tumour models and performed experiments. A.O. and N.M. conducted in vivo experimental design and work. B.E.M.L., D.A.H. and J.G. designed experiments and supervised the study. All authors discussed the work, and edited and commented on the manuscript.

Competing interests

D.A.H. is a co-founder with equity interest in Lime Therapeutics Inc., Selectin Therapeutics Inc., and Nine Diagnostics Inc.; is a member of the scientific advisory board of Concarlo Therapeutics Inc., Celine Therapeutics Inc., Nanorobotics Inc., and Mediphage Bioceuticals Inc.; and is a consultant for METIS Therapeutics Inc. B.M.L., D.A.H. and J.G. have filed a provisional patent in relation to some of the work in this paper. The other authors declare no competing interests.

Additional information

Extended data is available for this paper at <https://doi.org/10.1038/s41551-024-01248-w>.

Supplementary information The online version contains supplementary material available at <https://doi.org/10.1038/s41551-024-01248-w>.

Correspondence and requests for materials should be addressed to Jan Grimm.

Peer review information *Nature Biomedical Engineering* thanks Jianmin Wu and the other, anonymous, reviewer(s) for their contribution to the peer review of this work. Peer reviewer reports are available.

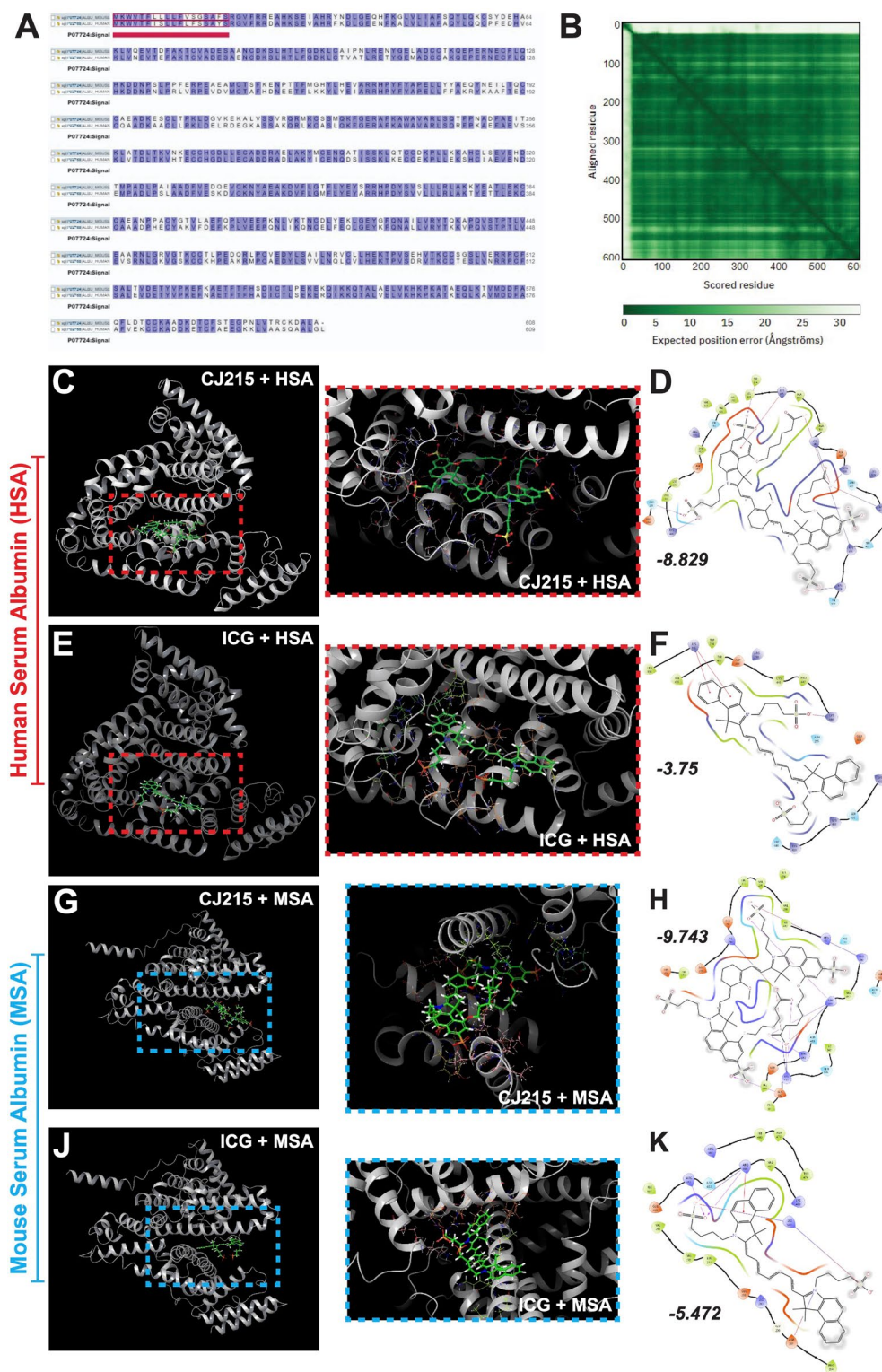
Reprints and permissions information is available at www.nature.com/reprints.

Publisher's note Springer Nature remains neutral with regard to jurisdictional claims in published maps and institutional affiliations.

Springer Nature or its licensor (e.g. a society or other partner) holds exclusive rights to this article under a publishing agreement with the author(s) or other rightsholder(s); author self-archiving of the accepted manuscript version of this article is solely governed by the terms of such publishing agreement and applicable law.

© The Author(s), under exclusive licence to Springer Nature Limited 2024

¹Molecular Pharmacology Program, Memorial Sloan Kettering Cancer Center, New York, NY, USA. ²Pharmacology Program, Weill Cornell Medical College, New York, NY, USA. ³Laboratory of Comparative Pathology, Memorial Sloan Kettering Cancer Center, Weill Cornell Medicine, and The Rockefeller University, New York, NY, USA. ⁴Department of Physiology, Biophysics, and Systems Biology, Weill Cornell Medicine, Cornell University, New York, NY, USA. ⁵Colorectal Service, Department of Surgery, Memorial Sloan Kettering Cancer Center, New York, NY, USA. ⁶School of Chemistry and Biochemistry, Georgia Institute of Technology, Atlanta, GA, USA. ⁷Department of Radiology, Memorial Sloan Kettering Cancer Center, New York, NY, USA. ⁸Department of Radiology, Weill Cornell Medical Center, New York, NY, USA. ⁹Molecular Imaging Therapy Service, Memorial Sloan Kettering Cancer Center, New York, NY, USA. ¹⁰These authors contributed equally: Ali Yasin Sonay, Elana Apfelbaum. ✉e-mail: grimmj@mskcc.org



Extended Data Fig. 1 | In silico assessment of serum binding affinity of CJ215 and ICG to human serum albumin (HSA) and mouse serum albumin (MSA).

A) Overview of ALIGN results between human and murine serum albumin revealed a sequence homology of 72.37%. **B)** Predicted aligned error for murine albumin (AF-P07724-F1). **C)** Left, overview of CJ215 docking pose with HSA. Right, zoomed in portion of docking site. **D)** Residue interactions of HSA with CJ215. **E)** Left, overview of ICG binding with HSA. Right, zoomed in view of the

binding site. **F)** Residue interactions of HSA with ICG. **G)** Left, overview of docking pose of CJ215 with MSA. Right, zoomed in view of the binding site. **H)** Residue interactions of CJ215 with MSA. **J)** Left, overview of ICG binding with MSA. Right, zoomed in view of the binding site. **K)** Residue interactions of ICG and MSA. For D, F, H, & K the non-covalent binding co-efficient (GlideScore) is shown in italics, where more negative binding correlates to a stronger binding and interaction. In all cases CJ215 showed improved binding efficacy to albumin over ICG.

Reporting Summary

Nature Portfolio wishes to improve the reproducibility of the work that we publish. This form provides structure for consistency and transparency in reporting. For further information on Nature Portfolio policies, see our [Editorial Policies](#) and the [Editorial Policy Checklist](#).

Statistics

For all statistical analyses, confirm that the following items are present in the figure legend, table legend, main text, or Methods section.

n/a Confirmed

- The exact sample size (n) for each experimental group/condition, given as a discrete number and unit of measurement
- A statement on whether measurements were taken from distinct samples or whether the same sample was measured repeatedly
- The statistical test(s) used AND whether they are one- or two-sided
Only common tests should be described solely by name; describe more complex techniques in the Methods section.
- A description of all covariates tested
- A description of any assumptions or corrections, such as tests of normality and adjustment for multiple comparisons
- A full description of the statistical parameters including central tendency (e.g. means) or other basic estimates (e.g. regression coefficient) AND variation (e.g. standard deviation) or associated estimates of uncertainty (e.g. confidence intervals)
- For null hypothesis testing, the test statistic (e.g. F , t , r) with confidence intervals, effect sizes, degrees of freedom and P value noted
Give P values as exact values whenever suitable.
- For Bayesian analysis, information on the choice of priors and Markov chain Monte Carlo settings
- For hierarchical and complex designs, identification of the appropriate level for tests and full reporting of outcomes
- Estimates of effect sizes (e.g. Cohen's d , Pearson's r), indicating how they were calculated

Our web collection on [statistics for biologists](#) contains articles on many of the points above.

Software and code

Policy information about [availability of computer code](#)

Data collection

SWIRFI data were collected using a dedicated SWIR system (IR-VIVO, Photon, ...) using the inbuilt Physpec software and acquisition scripts (laser triggering, exposure time setting, ...). Raw data were saved from this system as .h5 files. NIRFI data were collected using the commercial IVIS system (IVIS Spectrum, Perkin Elmer) in fluorescence mode according to ICG presets (745 excitation, 840 emission, f stop 1, lamp high, small binning). IVIS data were saved as standard for the system, and analyses were performed on the 'Luminescent' tiff files. Confocal microscopy was performed on a STELLARIS 8 microscope (Leica, USA) with image settings for polarized white light, DAPI and CJ215 visualization. Uptake assessment of CJ215 under reduced metabolic activity and induced apoptosis conditions were performed on a Odyssey CLx (Li-COR). Histological sections were 5- μ m thick unstained or H&E stained (Leica Autostainer, ST5010) and imaged using an automated slide scanner at 20x magnification (0.8 NA, 3DHistech, Budapest, Hungary) with representative images shown at 20x (SlideViewer, Version 2.5, 3DHistech). Immunohistochemistry for CC3 was performed on paraffin sections using a Leica Bond RX automated stainer. CC3 IHC images were acquired via an Olympus VS200 slides scanner and VS200 ASW 3.4.1 software (Evident Scientific, Hamburg, Germany) using a 20X/0.80NA objective to generate whole slide images with a pixel size of 0.2738 μ m. CC3 images are presented at various magnifications after visualization in QuPath (v0.4.4) and image export to Fiji/ImageJ2 (version 2.14.0/1.54g). Plasma interaction of CJ215 and ICG was assessed via docking studies using the Schrodinger suite (release 2022-3) with the crystal structure of human serum albumin (HSA, pdb entry 1AO6) and the predicted structure (alpha fold, AF-P07724-F1) of murine serum albumin (MSA).

Data analysis

SWIRFI .h5 data were converted to tiff files and automatically saved using custom macros comprised of in-built functions within Fiji/ImageJ2 (Version 1.54g). Following tiff conversion, the images were dark-noise subtracted, flat-field corrected, with bright and dark pixel removal (median filtering) again via an automated macro comprising of in-built functions within Fiji/ImageJ that has been previously described. Regions of interest (ROIs) were defined in ImageJ, with the mean, median, SD and location recorded for the tumour site, body and background-fluorescence-level estimates. Tabular results were saved as .csv files and imported to Excel for SNR and CNR quantification, as previously described. Line-profile analysis was performed in Fiji/ImageJ using the plot-profile function with resulting profiles stored as .csv

files. Graphing and statistical analysis were carried out in Prism (GraphPad Prism, Prism 9 and 10 for macOS), and the analyses used are described throughout the manuscript. Quantification for 4 vs 37C and Staurosporine and z-Vad-FMK was performed by ROI drawing within wells containing cells on the raw .tiff files in Fiji/ImageJ2, followed by normalization based on the average of the control group, with plotting also performed in Prism. Select H&E and CC3 whole-slide images were examined by a board-certified veterinary pathologist (S.M.). Cellular co-localization analysis was performed in Fiji/ImageJ2 using the following plugins: Iterative Deconvolve 3D ImageJ and Coloc 2.

For manuscripts utilizing custom algorithms or software that are central to the research but not yet described in published literature, software must be made available to editors and reviewers. We strongly encourage code deposition in a community repository (e.g. GitHub). See the Nature Portfolio [guidelines for submitting code & software](#) for further information.

Data

Policy information about [availability of data](#)

All manuscripts must include a [data availability statement](#). This statement should provide the following information, where applicable:

- Accession codes, unique identifiers, or web links for publicly available datasets
- A description of any restrictions on data availability
- For clinical datasets or third party data, please ensure that the statement adheres to our [policy](#)

Source data for the main figures are provided with this paper. The raw and analysed datasets generated during the study are available for research purposes from the corresponding author on reasonable request.

Research involving human participants, their data, or biological material

Policy information about studies with [human participants or human data](#). See also policy information about [sex, gender \(identity/presentation\), and sexual orientation](#) and [race, ethnicity and racism](#).

Reporting on sex and gender	<input type="text" value="The study did not involve human participants."/>
Reporting on race, ethnicity, or other socially relevant groupings	<input type="text" value="-"/>
Population characteristics	<input type="text" value="-"/>
Recruitment	<input type="text" value="-"/>
Ethics oversight	<input type="text" value="-"/>

Note that full information on the approval of the study protocol must also be provided in the manuscript.

Field-specific reporting

Please select the one below that is the best fit for your research. If you are not sure, read the appropriate sections before making your selection.

Life sciences Behavioural & social sciences Ecological, evolutionary & environmental sciences

For a reference copy of the document with all sections, see nature.com/documents/nr-reporting-summary-flat.pdf

Life sciences study design

All studies must disclose on these points even when the disclosure is negative.

Sample size	This study investigated the feasibility of SWIRFI and CJ215 to localize multiple tumour types across multiple mouse lines with the goal of using as few mice as possible, in line with good animal practice. Additionally, no e.g., survival comparisons were made between dye receiving or dye free mice, reducing the efficacy of power analysis. Sample sizes for each tumour line were utilized in line with previous experience and prior publications. For 4T1 (n=4, FoxN1nu, female), PC3-PSMA (n=4, NODSCID, male), CT26 (n=4, FoxN1nu, female), HT1080 (n=4, FoxN1nu, female), SW1222 (n=4, FoxN1nu, female) and wound-healing models (n=4, FoxN1nu, female), mice intravenously received CJ215 at 2mg/kg, n=20 mice in total. Additionally, one mouse per group (aside from the HT1080 group) did not receive any injection (n=5). For ICG comparison experiments, n=4 female FoxN1/nu mice were used, where again n=3 mice received ICG intravenously and one did not receive any injection. Additionally, n=5 female BALB/c nude mice were used to assess CJ215 biodistribution at 48 h post injection; again, n=4 received CJ215 and n=1 received no injection. The total number of mice used in this work was n=38. FoxN1nu mice were preferentially selected as they did not require hair depilation and permitted further non-invasive assessment of dye biodistribution. This was especially important for the wound healing model as hair depilation in other models had caused wounds and dye uptake.
Data exclusions	No data were excluded. For biodistribution analyses, background subtraction from organ values sometimes resulted in negative values, and in such cases the negative values were excluded so as to not artificially increase tumour-to-organ comparisons.
Replication	Replication for individual tumour lines was performed in multiple male and female mice. As the goal of the investigation was to assess the tumour-targeting capabilities of the dye, comparisons between male and female mice for individual tumour lines was not performed.
Randomization	No randomization was performed, as no longitudinal outcomes were assessed between, for example, mice undergoing surgery with or

Randomization	without the dye. Current mouse-housing guidelines permit 5 mice per cage. In situations where 4 mice received the dye and one did not, the four were chosen randomly (with no specific preference), with one mouse left as a negative control for, for example, autofluorescence comparison.
Blinding	No blinding was performed, as the same researcher performed the injections, imaging and analysis.

Reporting for specific materials, systems and methods

We require information from authors about some types of materials, experimental systems and methods used in many studies. Here, indicate whether each material, system or method listed is relevant to your study. If you are not sure if a list item applies to your research, read the appropriate section before selecting a response.

Materials & experimental systems

n/a	Included in the study
<input type="checkbox"/>	<input checked="" type="checkbox"/> Antibodies
<input type="checkbox"/>	<input checked="" type="checkbox"/> Eukaryotic cell lines
<input checked="" type="checkbox"/>	<input type="checkbox"/> Palaeontology and archaeology
<input type="checkbox"/>	<input checked="" type="checkbox"/> Animals and other organisms
<input checked="" type="checkbox"/>	<input type="checkbox"/> Clinical data
<input checked="" type="checkbox"/>	<input type="checkbox"/> Dual use research of concern
<input checked="" type="checkbox"/>	<input type="checkbox"/> Plants

Methods

n/a	Included in the study
<input checked="" type="checkbox"/>	<input type="checkbox"/> ChIP-seq
<input checked="" type="checkbox"/>	<input type="checkbox"/> Flow cytometry
<input checked="" type="checkbox"/>	<input type="checkbox"/> MRI-based neuroimaging

Antibodies

Antibodies used	For CC3 IHC staining after heat-induced epitope retrieval in a pH 6.0 buffer, anti-CC3 antibody (Cell Signaling 9661) was applied at a concentration of 1:250, followed by a polymer detection reagent kit according to the manufacturer's instructions (DS9800, Novocastra Bond Polymer Refine Detection, Leica Biosystems).
Validation	https://www.cellsignal.com/products/primary-antibodies/cleaved-caspase-3-asp175-antibody/9661

Eukaryotic cell lines

Policy information about [cell lines and Sex and Gender in Research](#)

Cell line source(s)	4T1: source ATCC (CRL-2539) HT1080: source ATCC (CCL-121) CT26: source ATCC (CRL-2638) PC3-PSMA: source ATCC (CRL-1435), transfected by the V Ponomarev lab at MSKCC and kindly obtained from them. SW1222: (GPA33-expressing human colorectal cancer cell line) was obtained via the Veach lab from the Ludwig Institute for Cancer Immunotherapy (New York, NY). Upon receipt of the SW1222 cell line, cultures were established with two passages and cryopreserved in small aliquots.
Authentication	All cells aside from SW1222 were authenticated using short tandem repeat (STR) analysis profiling.
Mycoplasma contamination	The cells were confirmed to be mycoplasma-free.
Commonly misidentified lines (See ICLAC register)	No commonly misidentified cell lines were used.

Animals and other research organisms

Policy information about [studies involving animals; ARRIVE guidelines](#) recommended for reporting animal research, and [Sex and Gender in Research](#)

Laboratory animals	Multiple male and female mice were used, including FoxN1nu (nude mice), NOD-SCID and BALB/c mice. The mice received food and water ad libitum, under a 12-h on/off light cycle, with 5 mice per cage with food. Details regarding mouse experiments are below with values presented as: Experiment type - Age when Injected (Days), Mean Weight of injected mice (in grams) and weight standard deviation (SD). 4T1 - 56 Days, 24.75g, SD: 1.92g CT26 - 91 Days, 22.00g, SD: 0.63g PC3-PSMA - 78 Days, 23.75g, SD: 1.48g
--------------------	--

HT1080 - 142 Days, 26.5g, SD: 0.87g
SW1222 - 125 Days, 24.75g, SD: 0.83g
Wound - 48 Days, 23.00g, SD: 0.71g
ICG 4T1 - 230 Days, 28.25g, SD: 2.39g
4T1 CJ215 @ 48H - 84 Days, 20.25g, SD: 1.09g

In summary, the mice had an average age of 106.75 days with a STD of 55.21 days. In total, mice had an average weight of 24.10g with a SD of 2.71g.

Wild animals

The study did not involve wild animals.

Reporting on sex

Both male and female mice were used and have been reported accordingly.

Field-collected samples

The study did not involve samples collected from the field.

Ethics oversight

All mouse handling, experimentation, imaging, and housing was performed according to NIH guidelines and via approved IACUC protocols at MSKCC.

Note that full information on the approval of the study protocol must also be provided in the manuscript.